One-Dimensional Modeling of Mercury Cadmium Telluride Photodetectors

Operated at Low Temperatures

by

Pradyumna Muralidharan

A Thesis Presented in Partial Fulfillment
of the Requirements for the Degree
Master of Science

Approved July 2011 by the
Graduate Supervisory Committee:

Dragica Vasileska, Chair
Priyalal S. Wijewarnasuriya
Yong-Hang Zhang

ARIZONA STATE UNIVERSITY

August 2011

ABSTRACT

The long wavelength infrared region (LWIR) and mid wavelength infrared region (MWIR) are of great interest as detection in this region offers a wide range of real time applications. Optoelectronic devices operating in the LWIR and MWIR region offer potential applications such as; optical gas sensing, free-space optical communications, infrared counter-measures, biomedical and thermal imaging etc. HgCdTe is a prominent narrow bandgap material that operates in the LWIR region. The focus of this research work is to simulate and analyze the characteristics of a $Hg_{1-x}Cd_xTe$ photodetector. To achieve this, the tool 'OPTODET' has been developed, where various device parameters can be varied and the resultant output can be analyzed. By the study of output characteristics in response to various changes in device parameters will allow users to understand the considerations that must be made in order to reach the optimum working point of an infrared detector.

The tool which has been developed is a 1-D drift diffusion based simulator which solves the 1-D Poisson equation to determine potentials and utilizes the results of the 1-D electron and hole continuity equations to determine current. Parameters such as absorption co-efficient, quantum efficiency, dark current, noise, Transit time and detectivity can be simulated. All major recombination mechanisms such as SRH, Radiative and Auger recombination have been considered. Effects of band to band tunnelling have also been considered to correctly model the dark current characteristics.

Dedicated to the memory of Kartik and Pratik

ACKNOWLEDGMENTS

This work has been wholly motivated by my mentor and guide, Dr. Dragica Vasileska, without whose support it would not have taken this form. Her patience in helping me understand new concepts, and more importantly, the trust she placed in my capability have played a significant role in shaping this work.

I am grateful to Dr. Priyalal S. Wijewaranasuriya and Dr. Yong-Hang Zhang for being a part of my Graduate Advisory Committe. I would like to extend my appreciation to the School of Electrical, Computer and Energy Engineering at Arizona State University for providing me this opportunity to pursue my Master's degree.

I would also like to thank Raghuraj Hathwar and Ganapathy Iyer for giving me the benefit of their wisdom.

TABLE OF CONTENTS

PAGE

LIST OF FIGURES ………………………………………………………….. viii

CHAPTER :

Chapter 1 : INTRODUCTION ………………………………………………. 1

1.1. Introduction …………………………………..……………………. 1

1.2. Optical Devices ……….…………………………….……………... 2

1.3. II-VI Materials …………..…………………………………………… 3

1.4. Types Of Photodetectors …….………………………………………. 5

1.4.1. Photoresistors …...……………..………………………………. 5

1.4.2. PN Diode ……………………...……………………………… 6

1.4.3. PIN Diode ……………………...…………………………… 10

1.4.4. Avalanche Photodetector …………...…………………………. 13

Chapter 2 : BASIC PHOTODETECTOR PARAMETERS …………………16

2.1. Introduction ……….…………………………………………….... 16

2.2. Quantum Efficiency ….…………….…………………………….. 18

2.3. Response Times and Responsivity …….…………………………… 23

2.3.1 Transit Time ….…………………………………………….... 23

2.3.2 RC Time Constant …..………………………………………. 26

2.3.3 Responsivity ………..…………………………………….. 27

2.4. Noise in Photodetectors …….……………………………………. 28

2.5. Detectivity …….…………………………………………………. 29

Chapter 3 : NUMERICAL MODELING OF PHOTODETECTORS ………31

0.1. Introduction …….………………………………………………... 31

CHAPTER PAGE

0.2. Poisson's Equation – Discretization and Implementation ……..…… 31

0.2.1. Normalization of the Poisson equation ……..………………… 33

0.2.2. Finite Difference Representation ……………..………………. 34

0.3. LU Decomposition method ……….…………………………….... 35

0.4. Successive Over Relaxation Method ……….……………………… 39

0.5. Electron and Hole Continuity Equation ……………….………… 42

0.6. Generation-Recombination Mechanism ……………….………… 47

0.6.1. Shockley-Read-Hall Recombination ….……………..………... 47

0.6.2. Radiative Recombination ………………...…………………. 52

0.6.3. Auger Recombination ………………………...…………….. 53

0.6.4. Optical generation ………………………...……………… 54

0.7. Optical Absorption Model ……………….………………………. 55

0.8. Flowchart of Simulation Program ……………………….………. 58

Chapter 4 : MODELING OF HgCdTe PHOTODETETORS ……..……….. 62

4.1. Material Properties …………………….…………………………. 62

4.1.1 Intrinsic Carrier Concentration ………………..………………. 62

4.1.2 Bandgap ……………………………..……………………. 64

4.1.4 Effective Masses ………………..………………………….... 66

4.1.4 Mobility …..………………………………………………..... 65

4.1.5 Permitivitty ……………………………………………....… 66

4.2. Simulation Characteristics …………………………………………. 67

4.2.1 I-V characteristics ……………………………….………. 67

4.2.2 Dynamic Resistance ……………………………….….. 71

4.3. NEP ……..……………………………………………………... 72

CHAPTER PAGE

4.4. Detectivity ……………………………………………………………….. 73

4.5. Carrier Freezeout …………………………………………………... 75

Chapter 5 : CONCLUSIONS AND FUTURE WORK ………………….… 77

REFERENCES ……………………………………………………………... 82

LIST OF FIGURES

FIGURES

1.1. Spectrum of Light ……………………………………………………. 4

1.2. The Energy Bandgap as a function of the Lattice Constant for some relevant narrow bandgap materials. [T.C McGill *et al.*] ………......……... 5

1.3. (a) Energy Band Diagram, Conduction band, Valence band and Fermi Level vs. Distance …………………….......……………………………. 7

1.3.(b) Electron and Hole densities vs. distance ……………………………... 8

1.3.(c) Electric Field vs. Distance …………………………………………… 8

1.4. Reverse Bias Electric Field vs. Distance ………………………………... 9

1.5.(a) Electric Field vs. Distance for a PIN diode ……………………….… 11

1.5.(b) Electron and Hole densities vs. distance for a PIN diode ………………………………………………........…………………. 11

1.5.(c) Electric Field vs. Distance ………………………………………….. 12

1.6.(a) Junction capacitance as function of reverse bias voltage …………..... 12

1.6.(b) Leakage current as a function of reverse bias voltage [C.C Bueno *et al.*] ……………………………………………………...….......…… 12

1.7. Temperature dependant dark current comparison between InGaAs and Ge pin Photodetector [Mizumoto *et al.*] ………………………………......... 13

FIGURES PAGE

1.8. Visualization of the Avalanche process ……………………………..… 14

Page

2.1. The history of the development of infrared detectors ………………..… 16

2.2. A p^+-i-n^+ structure with radiation incident on the intrinsic region …….. 19

2.3. Schematic representation of p-n junction photodiode ……………….... 20

2.4. Quantum Efficiency vs. Wavelength for $d < L_p$ …….……………….... 21

2.5. Quantum Efficiency vs. Wavelength for $d < L_p$ and $d > L_p$ ………...... 21

2.6. Depletion region QE for $Hg_{1-x}Cd_xTe$ with x=0.225 at 78 K ……..…… 23

2.7. 1-D node point visualization of the device ……………………………. 24

2.8. Electric Field vs. Distance in a p-n $Hg_{1-x}Cd_xTe$ photodetector with x=0.225 ……………………………………………………...……... 25

2.9. $C_{Depletion}$ and $C_{Diffusion}$ ..…..............…………………………………..... 26

2.10. Noise Current vs. Temperature ……………....……………………..... 27

3.1. Representation of Dirichlet and Neumann conditions on the node points of a device …………………………………………………….........…. 38

3.2. A hypothetical device with 6 node points ……………………….....… 39

3.3. All permutations of emission and capture events. (Courtesy Dr. Schroder) ……………………………………………………………….........…… 46

3.4. Auger Lifetimes vs. 1000/T for different doping densities …………… 53

3.5. Absorption Coefficient vs. Energy for $Hg_{1-x}Cd_xTe$ for x=0.225, 0.3 and 0.4 ………………………………………………………….............… 55

3.6.(a) Flowchart of simulation program …………………………………... 57

3.6.(b) Continuation of flow chart …………………………………….…..... 58

3.6.(c) Continuation of flow chart ………………………………….…..….. 59

FIGURES PAGE

3.6.(d) Continuation of flow chart …………………………………………….……. 60

4.1. Intrinsic Carrier Concentration vs. Temperature ………………………. 62

4.2. Intrinsic Carrier Concentration vs. Cadmium Mole Fraction (x) ……..... 62

4.3. Intrinsic Carrier Concentration vs. Mole fraction at 78 K, 100 K, 150 K, 250 K and 300 K …………………………………………….........…… 63

4.4. Bandgap vs. Mole Fraction at 78 K ……………………………….…. 64

4.5. Bandgap vs. Temperature at x=0.225 ………………………………..… 64

4.6. Dark Current Characteristics with Diffusion Region and Tunnelling region ………………………………………………….………........… 68

4.7. Dark Current Characteristics for $Hg_{1-x}Cd_xTe$ with x=0.225. p^+-n junction with $N_a = 2\times10^{16}$ cm^{-3} and $N_d = 10^{15}$ cm^{-3} ………………………..........… 69

4.8. Dark current with and without the tunnelling models ………………..… 69

4.9. Dynamic resistance vs Reverse Voltage ………………………………. 71

4.10. Detectivity vs. Wavelength ……………………………………….... 73

4.11. Detectivity vs. Wavelength at various temperatures ………………..… 74

4.12. p/N_a and n/N_d vs. temperature ……………...…………………..……. 75

4.13. $n,p/n_i$ vs. Temperature ……………………………………………... 75

5.1. Evolution of HgCdTe crystal growth technology from 1958 to the present ……………………………………………………………………............ 78

INTRODUCTION

1.1. Introduction

Semiconductors had been utilized in electronic devices for some time even before the invention of the transistor. They were commonly used as detectors in radios, which was also referred to as the ‘cat’s whiskers’ [1] device. This device was developed by Jagdish Chandra Bose, G.W Pickard and others. It could perhaps be the first true semiconductor device. The ‘cat’s whisker’ is a perfect example of a Shottky Diode. At the time it was discovered that it was quite an unreliable device whose working could be described as ‘mysterious’ at best. Since those early days our understanding of the operation of semiconductors devices has changed tremendously.

The true investigation of semiconductor devices only began in the 20th century, and the progress that has been made in the last century is nothing short of astounding. In the early days, researchers at Bell labs conducted a rigorous analysis of semiconductor behavior. The understanding of the basics of the PN diode led to the development of the PNP contact transistor. This device was the brainchild of two experimentalists and one theoretician, John Bardeen, Walter Houser Brattain and William Bradford Shockley. They developed the first transistor in 1947, and they eventually won the Noble Prize for this inaugural feat. William Shockley also further developed a special ‘sandwich’ structure which is now known as a bipolar junction transistor (BJT).

Since the turn of the century, various branches of science have begun to merge to realize their complete potential. This holds true for

semiconductors as well. The field of optics and semiconductor optoelectronics have come together to form many novel devices.

It is important to note that light and its properties have been known for a long time. But only recently have the knowledge of the light spectrum and the knowledge of semiconductor physics merged. Albert Einstein won the Noble Prize in 1921 for explaining the Photoelectric effect. Many modern devices are based on this concept, that light incident on a particular material is capable of providing energy to electrons. The Planck – Einstein equation tells us that

$$E = \frac{hc}{\lambda} \tag{1.1}$$

Where E is the energy of the incident photon, and lambda is the wavelength of the incident radiation. This tells us that radiation of shorter wavelength will have higher energy. This concept plays a major role in the operation of many semiconductor optoelectronic devices.

1.2. Optical Devices

A device that interacts with light by producing, measuring or manipulating light is said to be an optoelectronic device. The study of such devices and their behavior contributes to the field of Optoelectronics. These devices have various applications in various fields like medicine, sensing, imaging, security and many military applications as well.

Many silicon based detectors offer the ability to detect the entire visible spectrum of light. With Si and Ge based devices detection of the beginning of the infrared spectrum is possible, also known as the short

wavelength infrared region (SWIR). The primary interest of this research will be in the infrared spectrum of light. In that context infrared detectors are of enormous interest as the practical realization of optoelectronic devices operating in the 2-10 μm wavelength range offers potential applications in a variety of areas including optical gas sensing, environmental monitoring, free-space optical communications, infrared counter measures, clean energy generation, biomedical and thermal imaging. The mid-infrared region contains the fingerprint absorption bands for various pollutant and toxic gases. Operating in the MWIR (mid wavelength infrared region, 3-5 μm) enables free-space optical communication and thermal imaging applications in both civil and military situations. However, devices operating in the infrared region hitherto have not been able to reach their complete potential due to various challenges. II-VI materials have been utilized for this purpose. To operate in the LWIR (long wavelength infrared region, 8-14 μm), II-VI materials have been used but the immature fabrication techniques and incomplete understanding of their physical properties have stymied progress in this direction. The light spectrum is shown in Fig.1.1

1.3. II-VI Materials

II-VI materials have drawn a lot of interest over the years, as they have the capability to behave as a wide bandgap (1.5 eV – 3.5 eV) material as well as a narrow bandgap (0 eV – 1.5 eV) material. Wide bandgap materials include Zinc Selenide (ZnSe), Zinc Telluride (ZnTe), Cadmium Zinc Telluride (CdZnTe), Zinc Sulphide (ZnS) etc, whereas the narrow bandgap materials

include Mercury Cadmium Telluride (HgCdTe) and Mercury Zinc Telluride (HgZnTe).

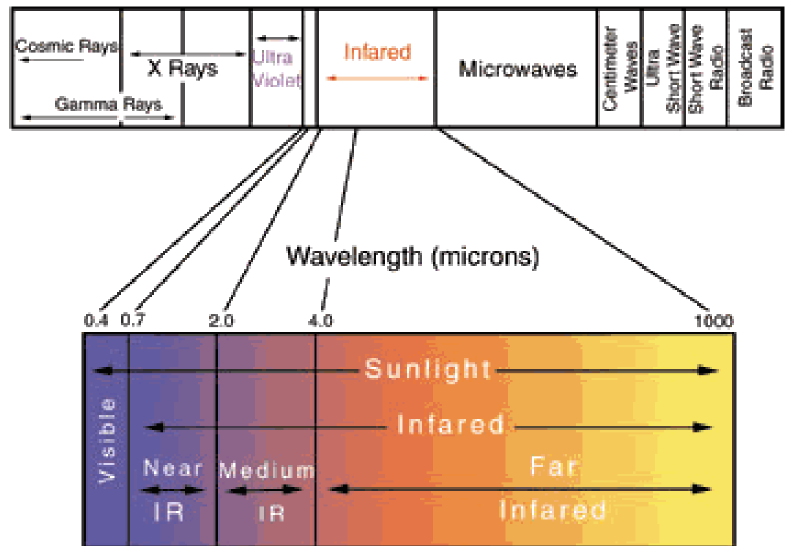

Fig.1.1: The Spectrum of light

Fig.1.2 shows us a grouping of materials with similar lattice constants. It is also clear that HgTe/CdTe are well matched material systems [2]. In the context a HgCdTe device, alloys of CdTe such as CdZnTe is used for epitaxial growth in molecular beam epitaxy.

The narrow bandgap materials have distinctive properties that can be utilized in novel device structures. Also, modern epitaxial techniques and the growing interest in nano structures have provided novel areas of application that utilize some of the unique properties of these materials. The materials with narrow bandgap can detect the entire visible spectrum of light as well as infrared radiation. The small effective mass in these materials make them ideal candidates to study quantum confinement.

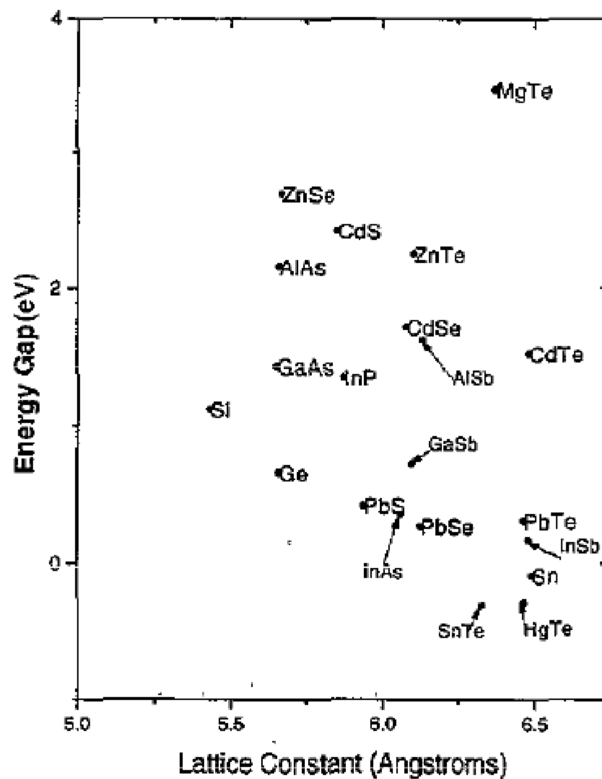

Fig.1.2: The Energy Bandgap as a function of the Lattice Constant for some relevant narrow bandgap materials. [T.C McGill *et al.*]

1.4. Types of Photodetectors

1.4.1. *Photoresistors*

A photoresistor is a device whose resistance decreases as the intensity of incident light increases. This device is also known as a Light Dependent Resistor (LDR). LDR's can be intrinsic or extrinsic; the difference between them being that the extrinsic device has impurities (dopants) present in them. When light of a particular energy falls on the device it can excite an electron from the valence band into the conduction band. This electron is now free to conduct electricity, thus lowering the resistance. In the early days photoresistors were made of Cadmium Sulphide (CdS) as they were economical to produce.

Different types of Photodetectors are used for different applications. CdS can be found in many consumer items such as alarm clock radios, camera light meters and street lights, etc. Lead Sulphide (PbS) and Indium Antimonide (InSb) photodetectors are used for detection in the mid-infrared spectral region.

1.4.2. *PN Diode*

In this section we will analyze the PN diode and it characteristics from the viewpoint of being an optical device. Consider a light source that is illuminating the PN diode. If the energy of the photons is greater than the band gap of the material, generation of electron hole pairs (EHP's) will take place. This generation process will occur throughout the whole structure including the depletion region of the pn junction. The depletion region of a pn junction is can be given as function of doping.

Depletion width W = $\sqrt{\frac{2\,K_S\,\varepsilon\,\,V_{bi}(N_A + N_D)}{qN_AN_D}}$; where V_{bi} is the built in potential, N_A is the p-type doping, N_D is the n-type doping, q is the fundamental charge, ε is the permittivity of free space and K_s is the relative permittivity.

For N_A>>N_D;

$$W = \sqrt{\frac{2K_s\varepsilon V_{bi}}{qN_D}} \qquad (1.2)$$

Equation 1.2 suggests that the depletion width is dominated by the light

doping. As the depletion region harbors most of the generation, it is essential that one maximizes the area of the space charge region.

Another important factor that must be taken into consideration is the internal electric field. As the incident radiation creates EHP's in the depletion region, the internal electric field must be high enough so that it can separate them. Otherwise they would just recombine within the space charge region and even though there was a generation event we would register zero photocurrent. Therefore even if every incident photon were to cause a 'generation event' (100% quantum efficiency), none of the generated electrons or holes would make it to the external contact. A higher doping for the p and n side would lead to higher internal electric field but would reduce the space charge region.

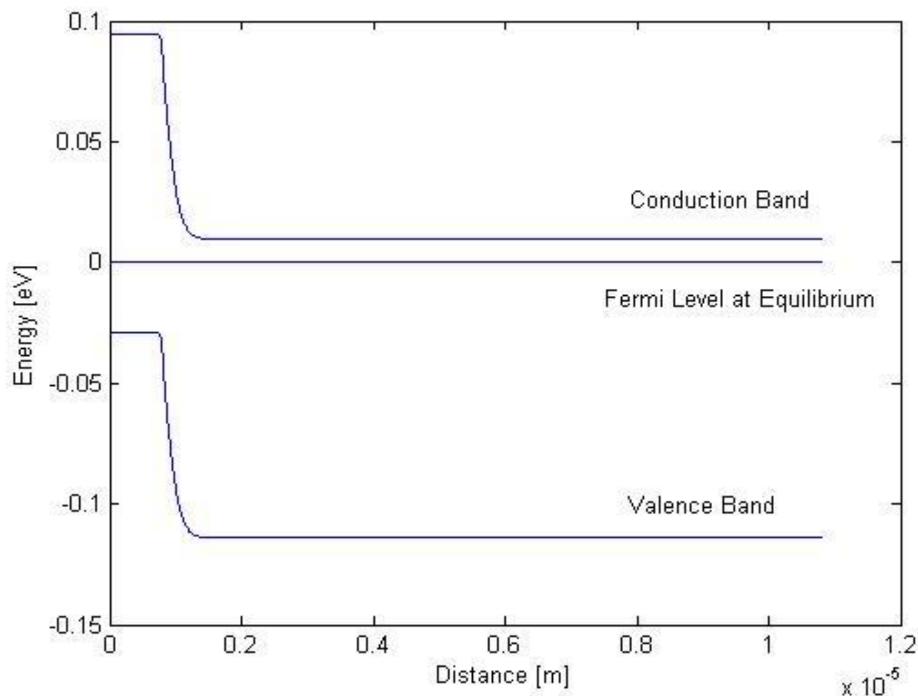

Fig.1.3 (a):Energy Band Diagram, Conduction band, Valence band and Fermi Level vs. Distance.

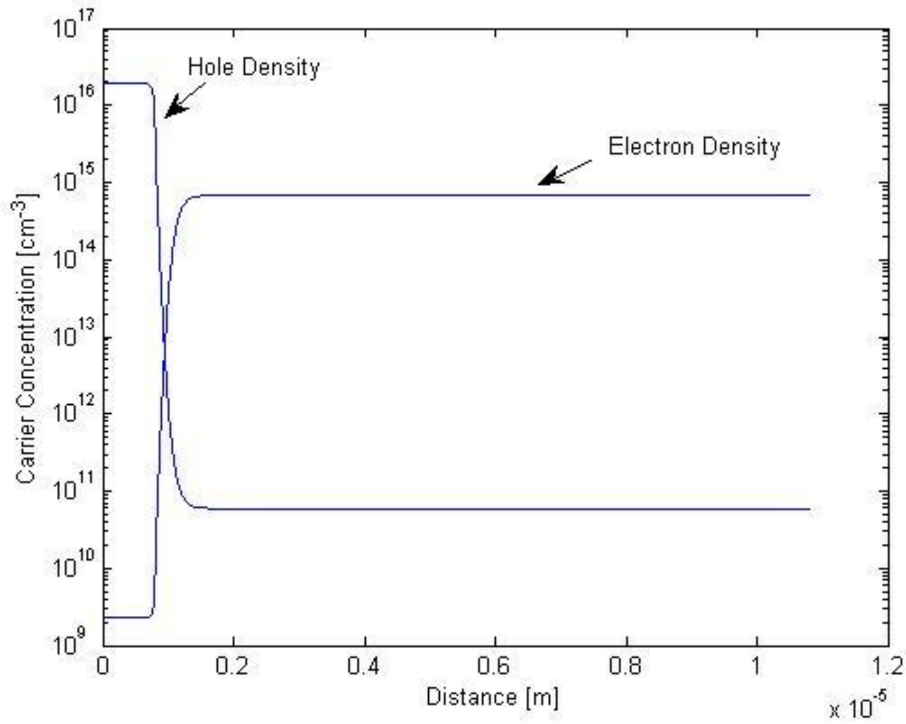

Fig.1.3 (b): Electron and Hole densities vs. distance.

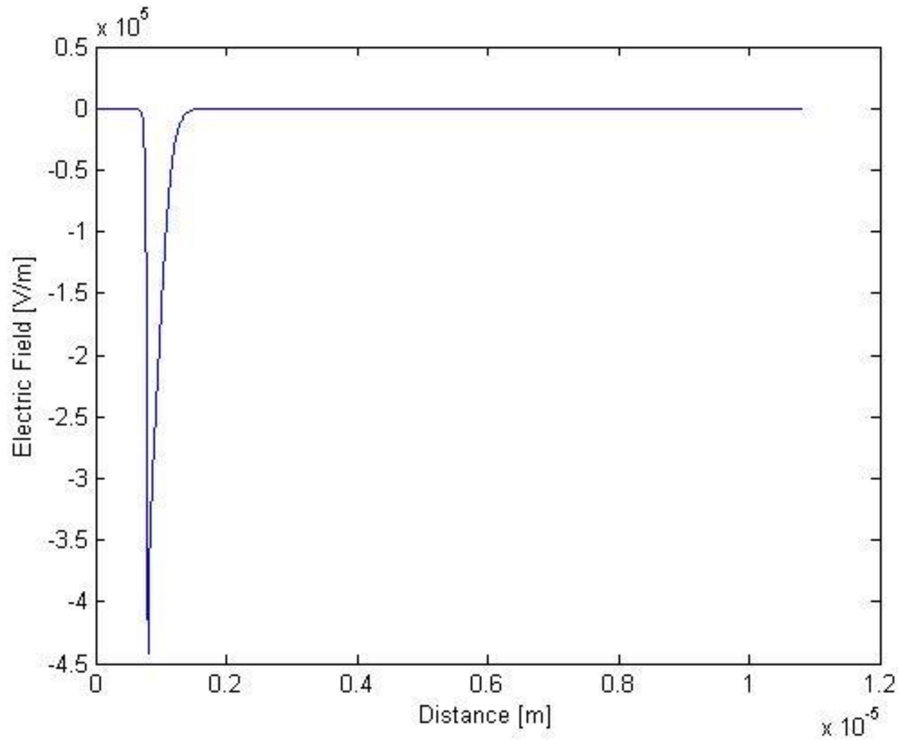

Fig.1.3(c): Electric Field vs. Distance.

All the results displayed in Fig.1.3(a), (b), (c) and 1.4 are for a $Hg_{1-x}Cd_xTe$ device with x=0.225 at 78 K. $N_A=2 \times 10^{16}$ cm^{-3}, $N_D=10^{15}$ cm^{-3}.

Operating the pn junction in reverse bias would lead to an increase in the space charge region as well as an increase in the electric field. This mode of operation is known as the *photoconductive mode.* This mode of operational also leads to a reduction of the junction capacitance, which leads to smaller RC constant. This leads to a faster response time as

$$\tau = \sqrt{RC}; \text{ where } \tau \text{ is the time constant}$$

However, the photoconductive mode does exhibit more distinct noise characteristics.

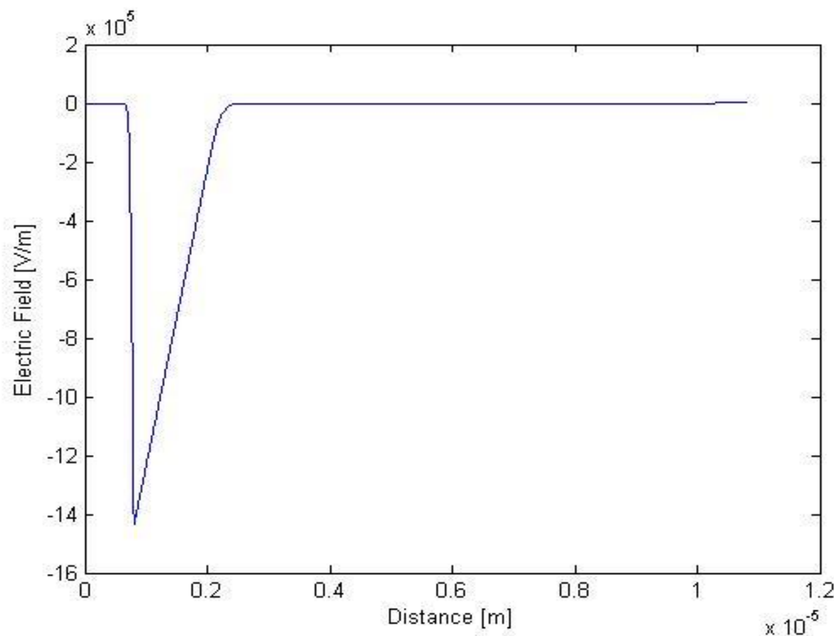

Fig 1.4: Reverse Bias Electric Field vs. Distance.

If we compare the reverse bias electric field in Fig.1.4, in which the device is under a reverse bias on -0.5 V to the electric field in Fig.1.3 (c), we observe that the field in the space charge region has increased. This is the internal electric field which helps separate the EHP's.

Operating in the *photoconductive* mode, does dramatically reduce transit times and the junction capacitance, but this method is more susceptible

to noise. As we have discussed earlier, to maximize the generation of electron hole pairs, we must increase the photosensitive area. An innovative way to achieve this is by inserting an intrinsic region between the p and n doped sides. We will discuss this device structure in the next section.

1.4.3. PIN Diode

Jun-ichi Nischizawa is credited for the invention of the PIN diode in 1950. This structure includes an ideal intrinsic layer sandwiched between the p and n doped side. The large intrinsic layer is completely depleted under reverse bias conditions which maximizes the photosensitive area where incident radiation can cause generation. In the previous pn structure, the high p^+ and n^+ doping would reduce the space charge region, but in a PIN structure, one can dope the p and n sides heavily. The intrinsic region remains depleted even with high doping on either sides as proven by the simulations.

Fig.1.5 (a), (b) and (c) shows the energy band diagram, carrier concentrations and electric field respectively of a p-i-n device, where $N_A=10_{16}$ cm^{-3}, $N_D=10^{16}$ cm^{-3} and the length of the intrinsic region is 6 μm. In a PIN structure the high doping doesn't affect the area of the space charge region; therefore one can simultaneously have a large photosensitive area as well as large electric fields which will help separate the generated EHP's. The PIN structure does offer a lot of advantages; the large depletion region reduces the junction capacitance which reduces the RC time constant. However the transit time does increase as the time taken to leave the intrinsic region and reach the contact will increase. Also due the size of the diode it takes longer to shut it 'off'.

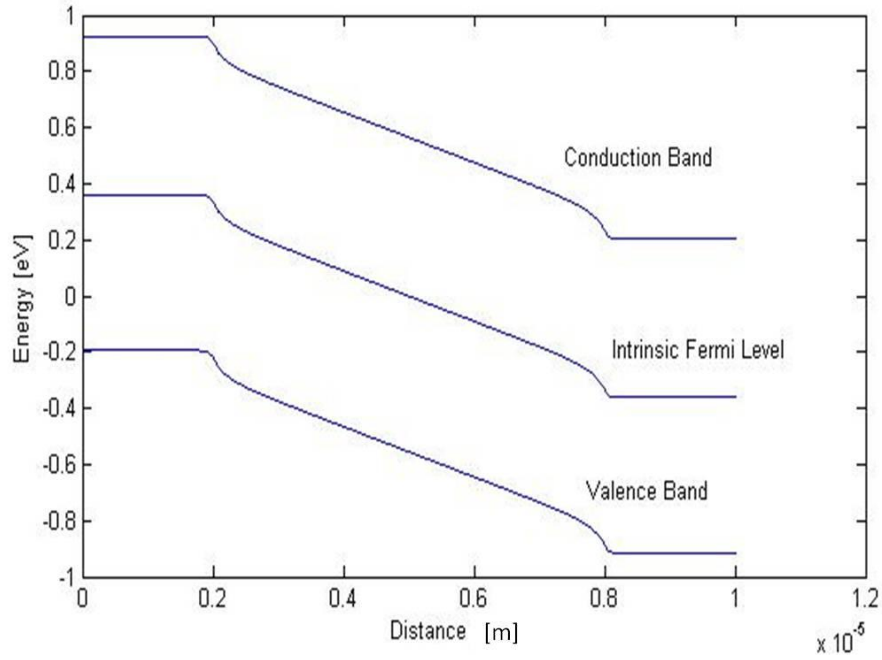

Fig.1.5 (a): Electric Field vs. Distance.

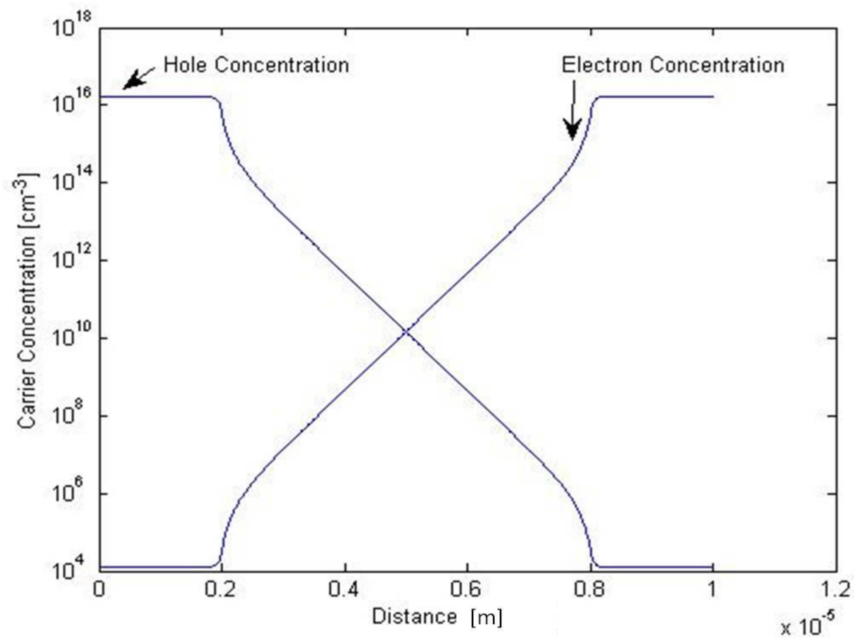

Fig.1.5 (b): Electron and Hole densities vs. distance.

The PIN structure does have many applications as RF and Microwave switches but we will limit ourselves to discussing its operation as a detector. As a detector it is used in the photoconductive mode, and the noise is distinctly lower in a p-i-n as opposed to a pn device. It exhibits very low

leakage currents. For silicon based PIN diode, leakage currents of the order of $\approx 10^{-7}$ A/cm^2 were obtained through simulations.

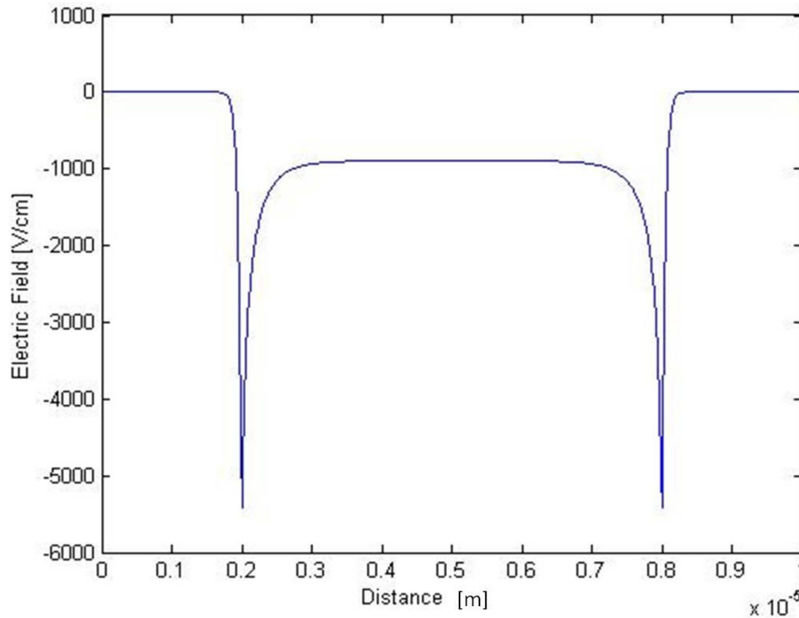

Fig.1.5 (c): Electric Field vs. Distance.

From the results represented in Fig.1.6 we observe that the Junction capacitance is a decreasing function of the reverse bias voltage and that the reverse bias leakage current $\approx 10^{-7}$A/cm^{-2}[3]. A reduction in capacitance will reduce the time constant but the transit time will still be heavily dependent on the space charge region area.

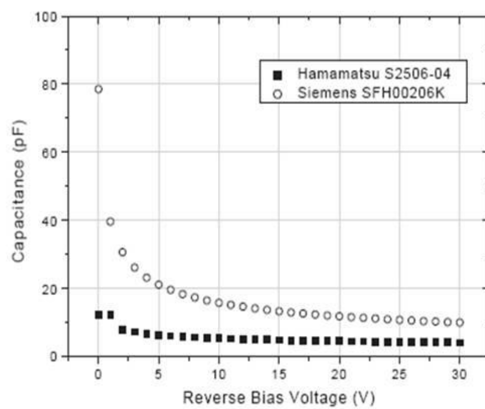

Fig 1.6 (a)

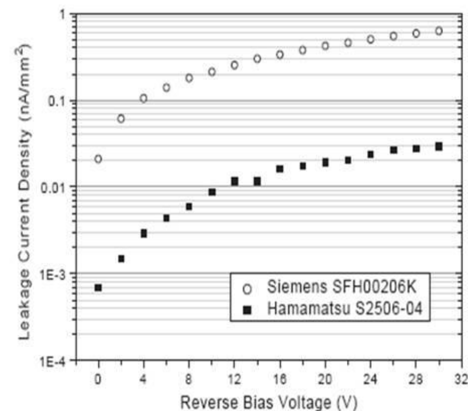

Fig 1.6(b)

In Fig 1.6:(a) we can see the Junction capacitance as function of reverse bias voltage, and (b) shows the leakage current as a function of reverse bias voltage [C.C Bueno *et al.*]

Many novel materials are used in the PIN configuration to function as a detector. An InGaAs PIN diode has been used for infrared detection in [4].

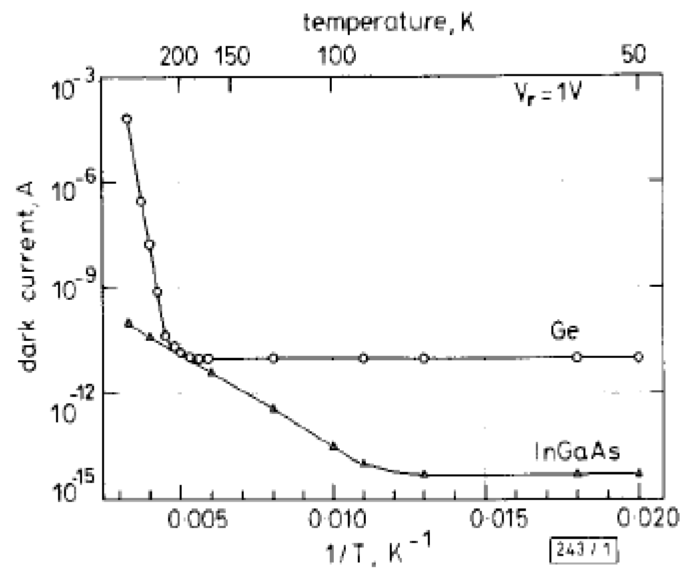

Fig 1.7: Temperature dependant dark current comparison between InGaAs and Ge pin Photodetector [Mizumoto *et al.*]

1.4.4 Avalanche Photodetector

An avalanche Photodetector is a device which utilizes impact ionization to induce carrier multiplication. As electrons enter the photodiode, they generate electron hole pairs if the Energy of the incident photon is greater than the bandgap of the material. An avalanche device is usually operated under heavy reverse bias so that a high field exists within the device. The electrons generated in the depletion region move towards the n-type side and the holes drift towards the p-type side. At a particular level of electric field the

generated electron will have sufficient energy to collide with the lattice atoms and ionize them thus creating more carriers. This process repeats rapidly increasing the number of carriers. This phenomenon is referred to as '*Avalanche Photocurrent*'.

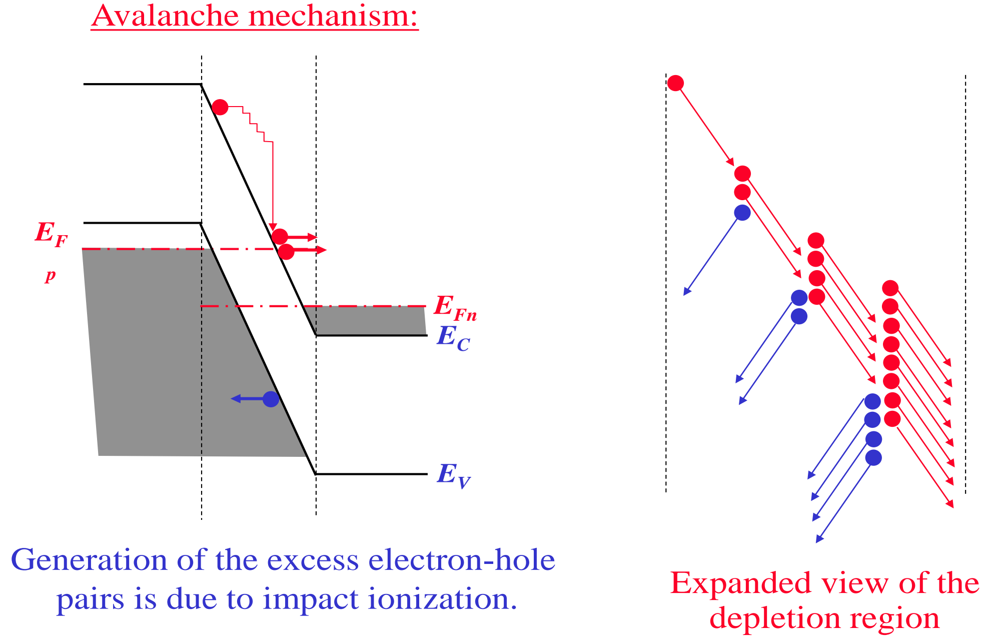

Fig.1.8: Visualization of the Avalanche process

The Avalanche Photodiode (APD) depends quite heavily on the quantum efficiency of the device. Also, the incident photons generate the primary carriers which cause avalanche multiplication. The current generated by an APD will have a multiplication factor as the numbers of carriers are multiplied under reverse bias. This factor M is given by

$$M = \frac{e^{-\int_0^x (\alpha-\beta)dx}}{1-\int_0^l \alpha e^{-\int_0^x (\alpha-\beta)dx'} dx} \quad \text{[Wasim Hussain } et\ al.\text{]} \tag{1.3}$$

Where α is the ionization rate for electrons and β is the ionization rate for holes.

An APD is very sensitive device; therefore while considering an avalanche photodiode, one must consider the noise it might generate. The shot noise in a APD is more than a standard photodiode, as the 'multiplication' will add statistical fluctuations to the noise calculations.

The response of an APD depends on the same factors as those of a standard photodiode. A thick space charge region leads to a low RC time constant. But the area of the structure will increase the transit time of the carriers, therefore a tradeoff usually has to be made in order to find the optimal working point of the device. APD is a high gain device as avalanche multiplication can be obtained at relatively low reverse bias voltages which also make it more controllable. The gain increases almost linearly with the reverse bias voltage. While this is partly true, at relatively low bias, after a particular voltage this property is no longer exhibited. At certain reverse bias voltage the gain starts dropping as a voltage drop develops across the device due to the series resistance.

The Avalanche Photodetector is often used for high bit rate, long haul fiber optic communications, etc., due to it high internal gain. Since the avalanche multiplication plays such a pivotal role in determining the gain, noise characteristics, optimizing the region where multiplication takes place will result in a more efficient device. Sub micron scaling of the multiplication has resulted in lower noise and a higher gain bandwidth product. Another novel way of optimizing the device is to obtain a novel multiplication region through '*Impact Ionization Engineering*'. This technique utilizes heterojunctions to achieve greater localization of impact ionization when compared to spatially uniform structures [6].

BASIC PHOTODETECTOR PARAMETERS

2.1. Introduction

The study of infrared detectors started in the 20th century. Detection in the infrared region has gained a lot of attention in recent decades due the numerous potential applications. The long wavelength infrared region (LWIR) and mid wavelength infrared region (MWIR) are of great interest as detection in this region offers a wide range of real time applications. Optoelectronic devices operating in the LWIR and MWIR region offer potential applications such as; optical gas sensing, free-space optical communications, infrared counter-measures, biomedical and thermal imaging etc. Tremendous progress has been made in the last decade in the field of infrared detection [7] but there are several challenges that still impede complete utilization of the potential offered by the infrared spectrum [8]. Progress in the Infrared detector technology to a large extent depends on the development of semiconductor infrared (IR) detectors. Semiconductor detectors are usually included in the class of photon detectors. Photon detectors can offer greater sensitivity and response times, but great care must be taken in designing the device [9].

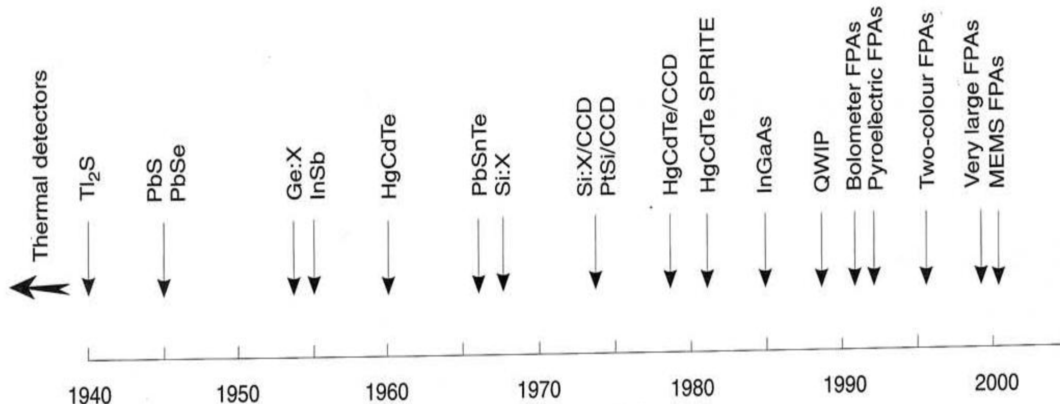

Fig 2.1: The timeline of the development of infrared detectors

To tap into the infrared spectrum many narrow bandgap materials have been investigated. Although the first widely used narrow-gap materials were lead salts during the 1950's, infrared detectors were built using single element cooled PbS and PbSe photoconductive detectors. In 1959, research by Lawson *et al.* [10] triggered the development of variable bandgap $Hg_xCd_{1-x}Te$ alloys providing an unprecedented degree of freedom on IR detector design. The fundamental properties of narrow bandgap semiconductors such as, high optical absorption, high electron mobility, fast response times and their compatibility for bandgap engineering make these materials the ideal choice for infrared detectors.

However, there are several obstacles in creating a high performance HgCdTe Photodetector. Fabrication of the material with the required purity in itself presents a unique challenge. Growth techniques such as liquid phase epitaxy (LPE) and molecular beam epitaxy (MBE) have been extensively researched to produce high purity HgCdTe. But despite major advances made in the past decades in these methods, various bulk growth techniques are still employed.

A major drawback of HgCdTe infrared detectors that operate in the long wavelength region (LWIR) is that they must be cooled down to very low temperatures to obtain high performance. Majority of the HgCdTe detectors must be operated at liquid nitrogen temperatures to obtain background limited performance (BLIP). Significant amount of research has been directed towards reducing the dark current of the device and trying to increase the device operating temperature, as operating at very low temperatures has a tremendous effect in increasing the operating cost.

In this chapter we will discuss some basic photodetector parameters that must be fine tuned so that the performance can be optimized. Quantum Efficiency, Responsivity, Response Times and Detectivity are some of the parameters that we will be discussing.

We also take a deeper look at the physics that takes place within the device which affect these parameters.

2.2. Quantum Efficiency:

Quantum efficiency (QE) is a very important parameter for photosensitive devices. It is a term that expresses the number of electron hole pairs (EHP) that are generated for every incident photon. The generated EHP’s which recombine at the contacts can be viewed as a simple picture of the radiation being detected. QE is often measured over a range of different wavelengths to characterize a device's efficiency at each photon energy. High quantum efficiency in a photosensitive device is imperative for obtaining high performance.

Quantum Efficiency depends on various factors and these are discussed below.

• ***Photosensitive Area***: The illumination is usually incident on a part of the device which is photosensitive. If the incident radiation is greater than the bandgap of the material, the energy of the radiation will be able to excite electrons into the conduction band, hence generating a electron hole pair. A larger photosensitive area would lead to larger number of EHP’s in the region, which leads to a higher quantum efficiency. The photosensitive area of a

device is usually the space charge region and the absorber region (lower doped region) of a device as show in Fig.2.2.

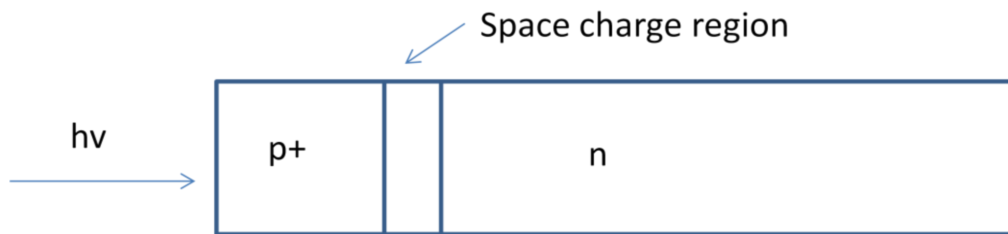

Fig 2.2: A p^+-n structure with front illumination

In Fig.2.2 we have a p^+-n structure where the p^+ region is degenerately doped and the n region which is the lower doped absorber side. Due to the high doping in HgCdTe photodetector, the space charge region is quite small. When EHP's are generated in the space charge region, the inherent electric filed that is present in the space charge region will separate the electrons and holes, while the EHP's generated in the quasi neutral region will diffuse to the contacts. Most photodiodes are designed so that most of the radiation is absorbed on one side of the junction. In Fig.2.24, this is the n-side of the junction. In theory, this could be achieved by making the p^+-region very thin or by using a heterojunction in which the p-region is in the wide bandgap configuration so that the incident radiation can reach the junction without being absorbed. The thickness of the illuminated junction (p^+-n in fig 2.2) must be small so that the radiation is not lost due to absorption by free carriers.

• ***Minority carrier diffusion Length*:** Consider figure 2.3. In this figure, the n-type region is the lower doped absorber region of thickness 'd'. If the back contact lies several minority carrier diffusion lengths 'L_p' (Hole diffusion

length in the n-type region), the quantum efficiency is then given by equation 2.1.(a).

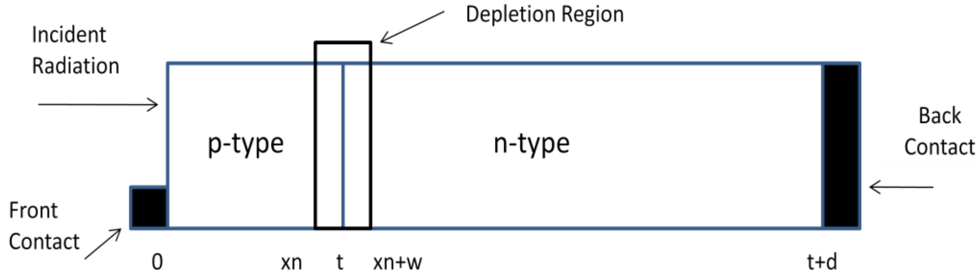

Fig 2.3: Schematic representation of p-n junction photodiode.

Therefore for $d > L_p$:

$$\eta = (1-R)\left[\frac{\alpha(\lambda)L_p}{1+\alpha(\lambda)L_p}\right] \tag{2.1 a}$$

where R is the Fresnel Coefficient. The Fresnel coefficient describes the reflection of light at the surface, α is the absorption coefficient. However, if the back contact is less than a diffusion length away from the junction, the quantum efficiency is given by equation 2.1.(b).

$$\eta = (1-R)\left[1-\exp\left(-\alpha\left(\lambda\right)d\right)\right] \tag{2.1 b}$$

where d is the thickness of the n-type region in fig 2.3.

In fig 2.4 we can see the quantum efficiency of a device with $d < L_p$. The thickness of the n side is 10 microns. Fig 2.5 shows the comparison of Quantum efficiency of a device with $d < L_p$ (d = 10 microns) and $d > L_p$ (d = 20 microns). For both the figures p^+ region was 0.8 microns with doping = 2 x 10^{17} cm^{-3} and the n side doping was 10^{15} cm^{-3}.

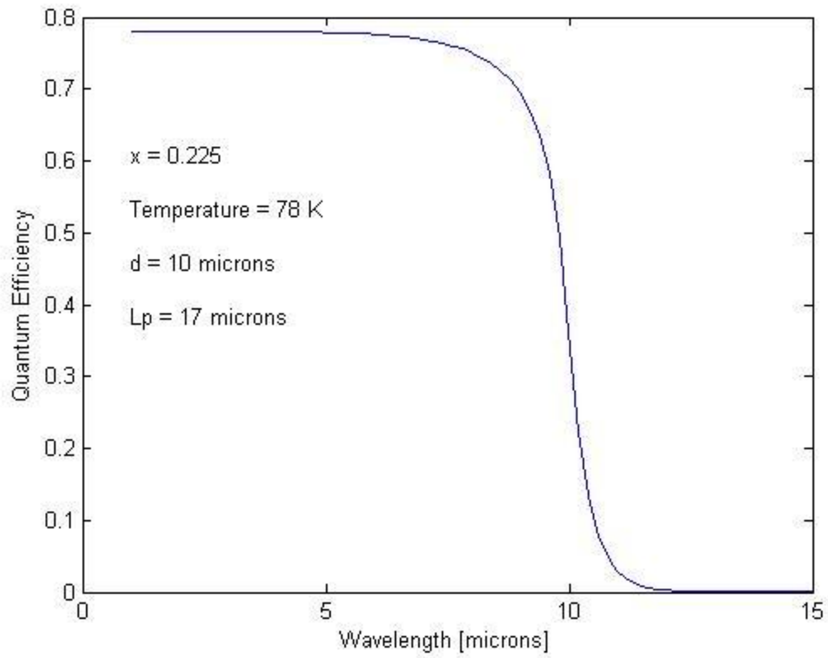

Fig 2.4: Quantum Efficiency vs. Wavelength, for $d < L_p$

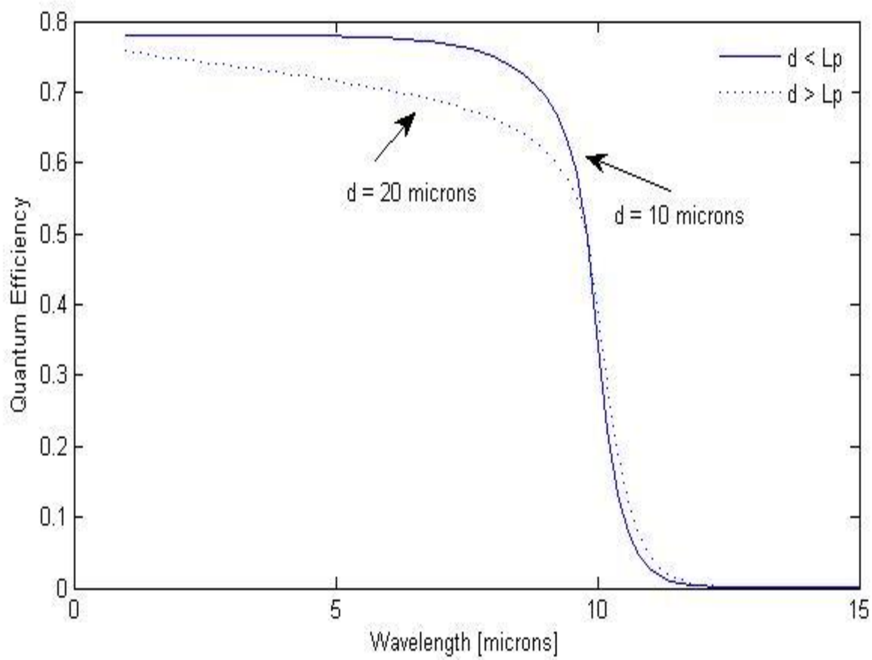

Fig 2.5: Quantum Efficiency vs. Wavelength, for $d < L_p$ and $d > L_p$.

We can see that for d > L_p the quantum efficiency reduces. This is due to the recombination of the generated EHP's in the bulk region of the low doped region.

Three regions contribute to the photodiode quantum efficiency, the two quasi neutral regions and the space charge region [11].

The n-side quantum efficiency is given by:

$$\eta_n = \frac{(1-R)\alpha L_h}{\alpha^2 L_h^2 - 1}\left\{ \frac{\alpha L_h + \gamma_1 - \exp(-\alpha x_n)\left[\gamma_1 + \cosh\left(\frac{x_n}{L_h}\right) + \sinh\left(\frac{x_n}{L_h}\right)\right]}{\gamma_1 \sinh\left(\frac{x_n}{L_h}\right) + \cosh\left(\frac{x_n}{L_h}\right)} - \alpha L_h \exp(-\alpha x_n) \right\}$$

(2.2)

where $\gamma_1 = s_1 L_h / D_h$, s_1 is the surface recombination velocity, L_h is the hole diffusion length and x_n is the n-side quasi neutral region [see Fig.2.4].

The p-side quantum efficiency is given by:

$$\eta_p = \frac{(1-R)\alpha L_e}{\alpha^2 L_e^2 - 1}\exp\left[-\alpha\left(x_n + W\right)\right] \times$$

$$\left\{ \frac{\left(\gamma_2 - \alpha L_e\right)\exp\left[-\alpha\left(t + d - x_n + W\right)\right] - \sinh\left(\frac{\left(t + d - x_n + W\right)}{L_e}\right) - \gamma_2 \cosh\left(\frac{t + d - x_n - W}{L_e}\right)}{\cosh\left(\frac{t + d - x_n - W}{L_e}\right) - \gamma_2 \sinh\left(\frac{t + d - x_n - W}{L_e}\right)} + \alpha L_e \right\}$$

(2.3)

The depletion region quantum efficiency is given by:

$$\eta_{DR} = (1-R)\left\{\exp\left(-\alpha x_n\right) - \exp\left[-\alpha\left(x_n + W\right)\right]\right\} \tag{2.4}$$

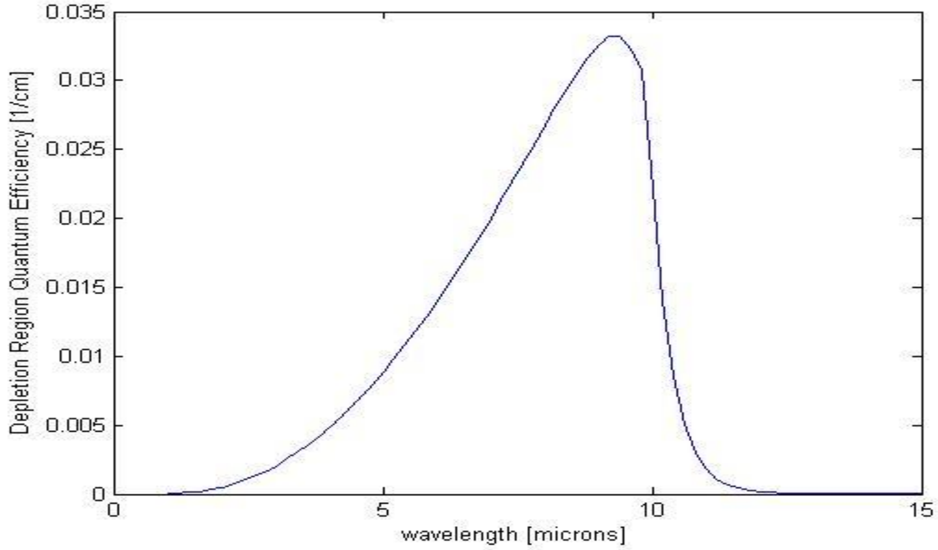

Fig 2.6: Depletion region QE for $Hg_xCd_{1-x}Te$ with x=0.225 at 78 K

In the equations 2.2, 2.3, 2.4 there is dependence of the quantum efficiency on the surface recombination velocity, but for all discussions in this thesis we will assume that the surface recombination velocity is 0. Therefore the aforementioned equations will reduce in complexity.

2.3. Response Times and Responsivity

2.3.1. *Transit Time*

As mentioned in previous sections, to design a high performance photodetector the interplay of various parameters has to be taken into consideration. To obtain the optimum values of all relevant parameters various

trade-offs need to made. There is considerable interest in fast response and high frequency photodetectors. This has been mostly due to LWIR applications at 10.6 μm for lidar systems and applications for optical fiber communications.

The frequency response of a photodiode is determined predominantly by three response parameters. Firstly by the time of carrier diffusion to the junction depletion region, secondly by τ_d; the transit time of the carrier drift across the depletion region, and thirdly by τ_{RC}; the RC time constant associated with circuit parameters including the junction capacitance C and the parallel combination of diode resistance and external load.

Fast response photodetectors are usually designed so that the absorption occurs in the p-type region. This ensures that most of the photocurrent is carried by electrons. Due to the low effective mass of electrons they generally exhibit a higher mobility.

The model used to calculate carrier drift time in the tool 'OPTODET' (which we will discuss in subsequent sections) is as follows. All discussions in this thesis are based on 1-D simulations. The entire device domain is divided into many node points as shown in Fig.2.7.

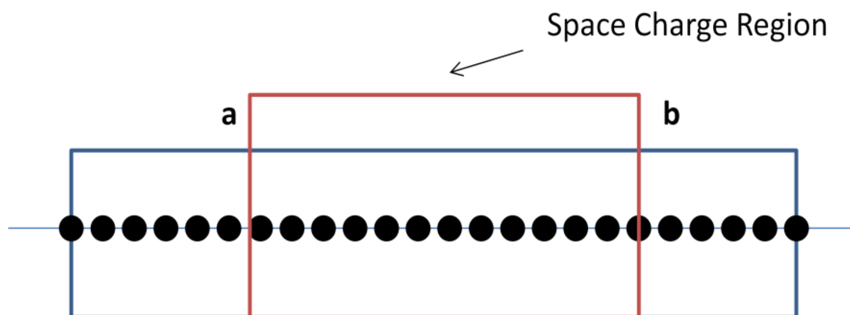

Fig 2.7: 1-D node point visualization of the device.

Let us consider the case of a p-n junction. As we described earlier, an electric field will exist in the space charge region as shown in Fig.2.8. From the knowledge of the mobility (μ) and the electric field (ϵ) at each node point, and the knowledge of the distance between successive node points, the carrier drift time between successive node points is calculated using the given formula:

$$\tau = \frac{d}{\mu \varepsilon_{avg}} \tag{2.5}$$

where d is the distance between successive node points and ϵ_{avg} is the average electric field between successive node points. By considering an average electric field we incorporate the influence of the space charge region electric fields even when the carrier is drifting in the quasi-neutral regions. We calculate τ for each node point from point 'a' to point 'b' in fig 2.7. The average of all the calculated $\tau's$ gives us the carrier drift time. It is obvious that when the junction is placed very close to the contact the transit times will be considerably lower compared to a device where the junction lies deep within the device. Thus, we can conclude that the transit time is primarily a function of the doping of the device and the bias applied. The doping of the device also determines the equilibrium space charge electric field and the length of the space charge region itself. A change in these parameters will result in a fluctuation of the transit time.

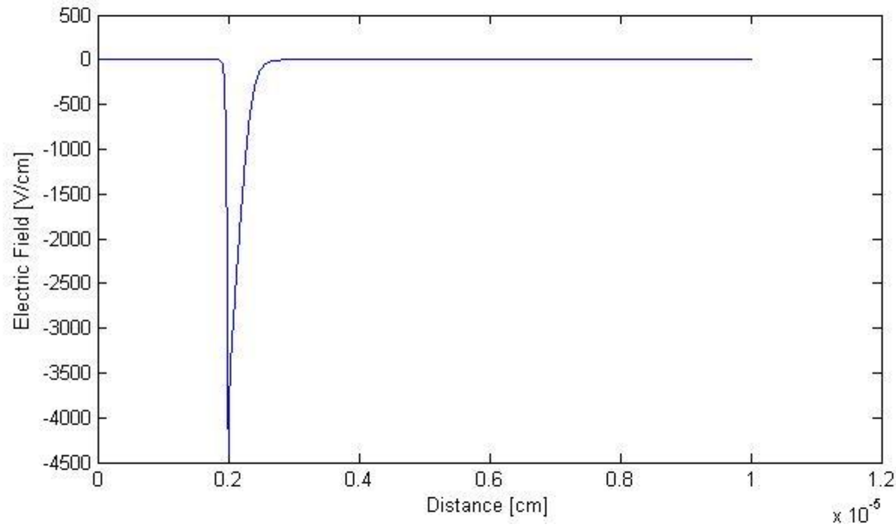

Fig 2.8: Electric Field vs. Distance in a p-n $Hg_xCd_{1-x}Te$ photodetector with x=0.225.

2.3.2. *RC Time Constant*

In practical scenarios, the most serious limitation in the operation of photodetectors arises from the RC time constant. The resistance capacitance product represents the RC time constant, which is the time required for the capacitor to charge up to 63% of its steady state value. However there are various components of capacitance and resistance that we must consider while calculating the time constant. In terms of the capacitance we must consider depletion capacitance and diffusion capacitance [12] which are in parallel, as shown in Fig.2.9.

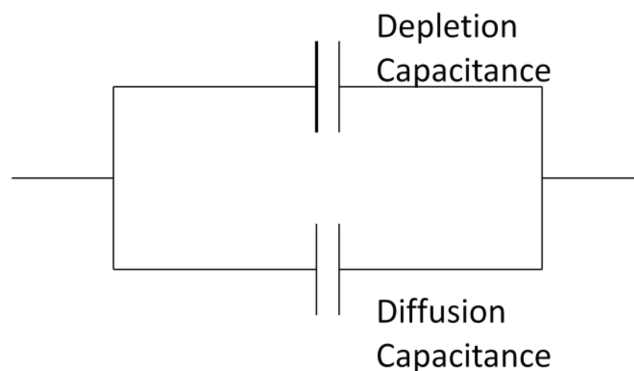

Fig 2.9: $C_{Depletion}$ and $C_{Diffusion}$ are in parallel.

Depletion capacitance is given by the expression:

$$C_{depl} = \sqrt{\frac{q\varepsilon_s N}{2}}\left[V_{bi} \pm V - \frac{2kT}{q}\right]^{-1/2}\left(\frac{F}{m^2}\right) \tag{2.6}$$

Diffusion capacitance is given by the expression:

$$C_{diff} = \frac{AqD_p p_{n0}}{2L_p V_T}\tau_p \exp\left(\frac{V_0}{V_T}\right) \tag{2.7}$$

Two important components of the resistance that have to be considered are the diode resistance and the load resistance.

2.3.3. *Responsivity*

An important figure of merit for photodetectors in the responsivity of the detector. It can be defined as the ratio of the photocurrent to the incident optical power. The expression for the responsivity of a photodetector is given by equation 2.8.

$$R = \frac{\eta\lambda q}{hc}(A/W) \tag{2.8}$$

where η is the quantum efficiency, q is the fundamental unit of charge, h is the planc's constant, c is the speed of light and λ is the wavelength of the radiation in microns. Therefore, for a given quantum efficiency, the responsivity increases linearly with wavelength.

2.4. Noise in Photodetectors

Any LWIR detector suffers from the problem of noise. This is one of the major concerns that affect the detectors performance. Thus, it becomes imperative to operate the detector at lower temperatures to reduce noise. However, by using this approach, one increases the operating cost.

The noise generated by a detector, operating under reverse bias, is a combination of shot noise, and Johnson noise. Shot noise occurs in optical detectors due to thermal noise mechanisms. The fluctuations in the velocities of free carriers due to their random motion and due to randomness in the rates of thermal generation and recombination jointly give rise to shot noise. The expression for shot noise is given by equation 2.9.

$$I_s = \sqrt{2qI_dB} \tag{2.9}$$

where I_d is the dark current and B is the Bandwidth.

The Johnson noise contribution is provided by the shunt resistance of the device, series resistance and the load resistance at zero bias. The Johnson noise is given by:

$$I_J = \left(\frac{4kTB}{R}\right)^{1/2} \tag{2.10}$$

In Fig 2.9 we can see the Shot Noise and Johnson Noise variation with temperature. The amount of shot noise also depends on the reverse bias voltage applied .In an ideal photodiode one can assume that the current will be diffusion limited, but in real life, especially for narrow bandgap materials, there are several other mechanisms which are heavily involved in determining the dark current vs. voltage characteristics. Apart from diffusion current in the quasi neutral regions and generation-recombination current in the depletion region, there are other mechanisms that are significant as well. This will be discussed in greater detail in chapter 3 and chapter 4.

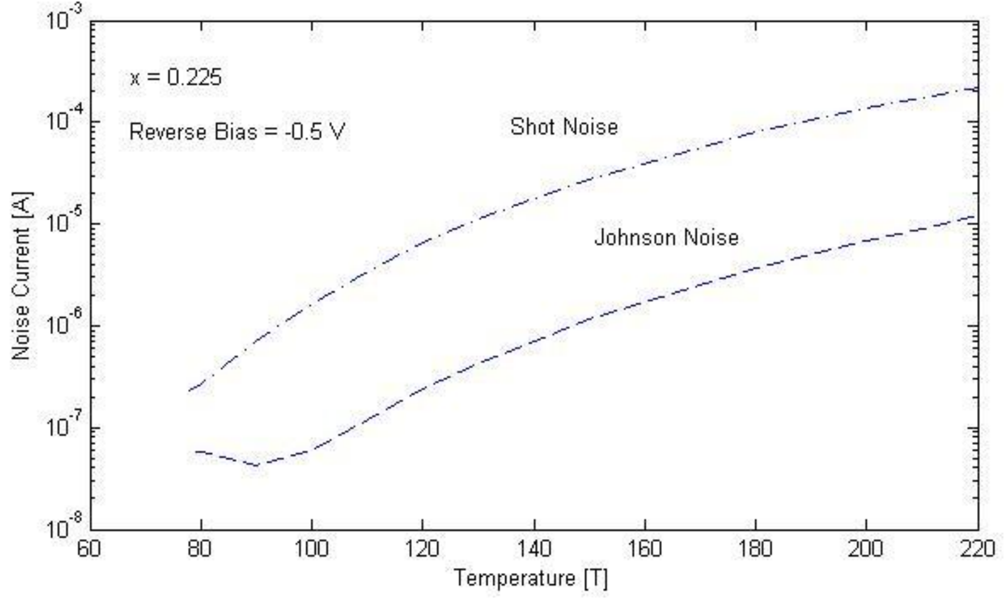

Fig 2.10: Noise Current vs. Temperature.

2.5. Detectivity

Detectivity is one of the prime figures of merit against which the performance of a detector is judged. The detectivity is given by the expression:

$$D^{*} = \frac{n\lambda q}{hc}\left[\frac{4kT}{RA} + 2q^{2}\eta P_{OPT}\right]^{-2} \quad (2.11a)$$

where λ is the wavelength, η is the quantum efficiency, P_{OPT} is the incident optical power density and R is the effective dynamic resistance.

$$\frac{1}{R_{eff}} = \frac{1}{R_{0}} + \frac{1}{R_{L}} \quad (2.11b)$$

where R_0 is the zero bias dynamic resistance and R_L is the load resistance.

As we know to majority of the infrared detectors must be operated at liquid nitrogen temperatures to obtain background limited performance (BLIP). In relation to equation 2.11a, two important cases must be outlined.

- For background-limited performance: $\frac{4KT}{R_0 A} << 2q^2\eta P_{OPT}$

- Thermal noise limited performance: $\frac{4KT}{R_0 A} >> 2q^2\eta P_{OPT}$

For an ideal photodiode the performance can be maximized by maximizing the quantum efficiency and minimizing the reverse saturation current. A higher R_0A product too will lead to higher detectivity. By now we have established that the leakage current that exists in a LWIR photodetector reduces the detectivity. There are a few design strategies that can be used to reduce the leakage current. They will be discussed in chapter 4.

NUMERICAL MODELING OF PHOTODETECTORS

3.1. Introduction

As the semiconductor technology continues to evolve, numerical modelling of semiconductor devices becomes an indispensible tool for the prediction of the electrical characteristics of the device. This thesis deals with the development of the tool 'OPTODET'. This tool has been developed to investigate and explain the device characteristics of HgCdTe Photodetectors at low temperatures. OPTODET is a 1-D drift-diffusion simulator. Complete Fermi-Dirac statistics have been implemented to contend with cases with degenerate doping. The devices that the tool simulates are all abrupt junction devices, in other words the doping in all regions is uniform. All simulations assume parabolic shaped bands. In this chapter we will take a closer look at the numerical methods which are used to solve Poisson's equation and the current continuity equations.

A drift diffusion simulator utilizes solutions of the Poisson's equation and the current continuity equations to determine the current flowing through the device.

3.2. Poisson's Equation – Discretization and Implementation

In order to solve for the potentials within the device one has to solve the Poisson's equation which is given by the expression:

$$\nabla^2.\phi = -\frac{e}{\varepsilon}(p - n + N_D^+ - N_A^-) \tag{3.1}$$

where φ is the spatially varying potential, e is the fundamental charge, ϵ is the permittivity, p and n are the electron and hole densities and N_D^+ and N_A^- are the

ionized impurities. Since we consider complete Fermi-Dirac statistics *n* and *p* are given by the following expressions:

$$n = N_C f_{1/2}\left[\frac{E_F - E_C}{kT}\right] \quad (3.2a)$$

$$p = N_V f_{1/2}\left[\frac{E_V - E_F}{kT}\right] \quad (3.2b)$$

where N_C and N_V are the effective conduction and valence band density of states. E_F is the Fermi energy, E_C is the conduction band energy, E_V is the valence band energy, k is the Boltzmann's constant and T is the temperature. The implementation of the $f_{1/2}$ integral will be discussed in greater detail in subsequent sections.

The effective conduction and valence band density of states is give by expression:

$$N_C = 2[\frac{2\pi m_e^* kT}{h^2}]^{3/2} \quad (3.3a)$$

$$N_V = 2[\frac{2\pi m_h^* kT}{h^2}]^{3/2} \quad (3.3b)$$

The solution of equation 3.1 using a computer program would require finite difference discretization so that the equation under analysis can be transformed in to a matrix equation. Then the equation can be solved using a numerical method such as the Successive over relaxation method (SOR) or the LU decomposition technique. In subsequent sections both techniques will be explained as both techniques have been implemented in OPTODET.

3.2.1 *Normalization of the Poisson Equation*

Under equilibrium conditions n and p are given by equation 3.2a and 3.b. Now consider the 1-D Poisson equation given by equation 3.4.

$$\frac{d^2\phi}{dx^2} = -\frac{e}{\varepsilon}(p - n + N_D^+ - N_A^-) \tag{3.4}$$

Let n and p be defined by the equations 3.5a and 3.5b

$$\begin{aligned} n &= n_i \exp\left(\frac{\phi}{V_T}\right) \\ p &= n_i \exp\left(-\frac{\phi}{V_T}\right) \end{aligned} \tag{3.5}$$

Assuming $\varphi => \varphi + \delta$, applying $e^{\pm\delta x} = (1 \pm \delta)$ and substituting this in the RHS and using $(N_d - N)_a / n_i = C$, one arrives at

$$\frac{d^2\phi}{dx^2} = -\frac{en_i}{\varepsilon_0}\left(\exp(-\varphi/V_T) - \exp(\varphi/V_T) + C\right) + \frac{en_i\delta}{\varepsilon_0 V_T}\left(\exp(-\varphi/V_T) + \exp(\varphi/V_T)\right) \tag{3.6}$$

Now, let the new value of φ be denoted as φ_{new} and the present value of φ be denoted as φ_{old}. Substituting $\delta = \varphi_{new} - \varphi_{old}$, we get

$$\begin{aligned} \frac{d^2\varphi^{new}}{dx^2} - \frac{en_i}{\varepsilon}\left(e^{-\varphi/V_T} + e^{\varphi/V_T}\right)\varphi^{new} &= -\frac{en_i}{\varepsilon}\left(e^{-\varphi^{old}/V_T} - e^{\varphi^{old}/V_T} + C/n_i\right) - \\ &- \frac{en_i}{\varepsilon}\left(e^{-\varphi^{old}/V_T} + e^{\varphi^{old}/V_T}\right)\varphi^{old} \end{aligned} \tag{3.7}$$

Rewriting in terms of p and n we get,

$$\frac{d^2\varphi^{new}}{dx^2} = -\frac{en_i}{\varepsilon}(p - n + C/n_i) + + \frac{en_i}{\varepsilon}\delta(p + n)$$

(3.8)

Now normalize x_i with L_D, and φ_i with V_T, where L_D is the intrinsic Debye length. This leads to

$$\frac{d^2\varphi^{new}}{dx^2} - (p+n)\varphi^{new} = -(p-n+C) - (p+n)\varphi^{old}$$

(3.9)

This is the normalized form of the Poisson equation.

3.2.2 *Finite difference representation*

Equation 3.9, though normalized is still in a differential form. The next step is to apply a finite difference approximation scheme to this equation. By applying the central difference formula, we get equation 3.10.

$$\frac{1}{\Delta^2}\varphi_{i+1}^{n+1} - \left(\frac{2}{\Delta^2} + n_i + p_i\right)\varphi_i^{n+1} + \frac{1}{\Delta^2}\varphi_{i-1}^{n+1} = -(p_i - n_i + C_i) - (p_i + n_i)\varphi_i^n$$

(3.10)

where 'i' represents the grid point, 'n' represents the iteration number and Δ is the normalized grid spacing. The finite difference Discretization of the 1D Poisson's equation leads to tridiagonal square input matrix (of the potential in the Poisson's equation). That is, the Poisson equation can now be represented as,

$$[A][\varphi] = [F]$$

(3.11)

Where F is the forcing function (which is essentially the RHS of Equation 3.11). The solution of the matrix equation is explained in the following section. We have utilized two numerical methods to solve equation

3.11, namely the successive over relaxation method and the LU decomposition method.

3.3. LU Decomposition method

A square matrix equation as in Equation 3.11, can be solved by breaking the tridiagonal square matrix $[\mathrm{A}]$ into lower triangular and upper triangular matrices, say $[L],[U]$ matrices, if the matrix is non-singular (in this case if there exists an inverse for the square matrix $[\mathrm{A}]$ such that $[\mathrm{A}][\mathrm{A}]^{-1}=1$ [Weisstein]. Also an invertible matrix admits LU Decomposition if and only if all its leading diagonal principal minors are non-zero. The factorization is unique if we require that the diagonal of L (or U) consists of ones. Both these conditions are satisfied in the discretized Poisson's equation Matrix representation.

Thus, one can write,

$$[\mathrm{A}]=[L][U] \tag{3.12}$$

Here $[L],[U]$ are the lower and upper triangular square matrices (of the same size), meaning that L has only zeros above the diagonal, and U has zeros below the diagonal. Thus Equation (3.12) transforms into,

$$[\mathrm{A}][\phi]=[L][U][\phi]=[F] \tag{3.13}$$

The solution for $[\varphi]$ can be found by expressing

$$[V]=[U][\phi] \tag{3.14}$$

Equation (3.14) changes into,

$$
\begin{aligned}
&[\mathrm{A}][\phi]=[L][V]=[F] \\
&\Rightarrow[L][V]=[F]
\end{aligned}
\tag{3.15}
$$

Thus $[V]$ has to be first solved, following which $[\varphi]$ can be solved from Equation (3.15). In order to do this, the $[L],[U]$ matrices have to be computed. This is accomplished in the following manner,

First, the coefficient matrix of the Poisson's equation is expressed as,

$$
\overset{\mathrm{A}}{\Downarrow}\qquad\qquad\qquad\overset{L}{\Downarrow}\qquad\qquad\qquad\overset{U}{\Downarrow}
$$

$$
\begin{pmatrix}
g_1 & c_1 & & & \\
e_2 & g_2 & c_2 & 0 & \\
 & \cdots & \cdots & \cdots & \\
 & 0 & e_{n-1} & g_{n-1} & c_{n-1} \\
 & & & e_n & g_n
\end{pmatrix}
=
\begin{pmatrix}
1 & & & & \\
\beta_2 & 1 & & 0 & \\
 & \cdots & \cdots & & \\
 & 0 & \beta_{n-1} & \cdots & \\
 & & & \beta_n & 1
\end{pmatrix}
\begin{pmatrix}
\alpha_1 & c_1 & & & \\
 & \alpha_2 & c_2 & 0 & \\
 & & \cdots & \cdots & \\
 & 0 & & \cdots & c_{n-1} \\
 & & & & \alpha_n
\end{pmatrix}
\tag{3.16}
$$

In the above matrix equation, the coefficients from Equation (3.10) form tridiagonal matrix which is decomposed into lower and upper triangular matrices.

To get the values of α, β, one could express the elements g_k, c_k, e_k in terms of α, β so that a general expression can be obtained for α, β. Thus from Equation (3.16) one has,

$$
\begin{aligned}
&g_1=1\times\alpha_1 \\
&\Rightarrow\boxed{\alpha_1=g_1}
\end{aligned}
\tag{3.17}
$$

Then based on this value of α_1, the β values are found from,

$$e_2 = \beta_2 \alpha_1$$
$$\Rightarrow \beta_2 = \frac{e_2}{\alpha_1} \tag{3.18}$$
$$\Rightarrow \boxed{\beta_k = \frac{e_k}{\alpha_{k-1}}}$$

Where $0 < k < n$, and n is the order of the matrix (in this case the number of mesh points)

Continuing the same gives,

$$g_2 = \beta_2 c_1 + 1\alpha_2$$
$$\Rightarrow \alpha_2 = g_2 - \beta_2 c_1 \tag{3.19}$$
$$\Rightarrow \boxed{\alpha_k = g_k - \beta_k c_{k-1}}$$

This gives us the entire $[L]$ and $[U]$ matrices. To solve Equation (3.15), rewrite the matrices as,

$$\overset{F}{\Downarrow}\begin{pmatrix} f_1 \\ f_2 \\ \cdots \\ \cdots \\ f_n \end{pmatrix} = \overset{L}{\Downarrow}\begin{pmatrix} 1 & & & & \\ \beta_2 & 1 & & 0 & \\ & \cdots & \cdots & & \\ & 0 & \beta_{n-1} & \cdots & \\ & & & \beta_n & 1 \end{pmatrix} \overset{V}{\Downarrow}\begin{pmatrix} v_1 \\ v_2 \\ \cdots \\ \cdots \\ v_n \end{pmatrix} \tag{3.20}$$

By forward substitution similar to the above procedure,

$$f_1 = 1 \times v_1$$
$$\Rightarrow \boxed{v_1 = f_1} \tag{3.21}$$

Then based on this value of v_1, one can obtain the entire $[V]$ from,

$$
\begin{aligned}
& f_2 = \beta_2 v_1 + 1 \times v_2 \\
& \Rightarrow v_2 = f_2 - \beta_2 v_1 \\
& \Rightarrow \boxed{v_i = f_i - \beta_i v_{i-1}}
\end{aligned} \tag{3.22}
$$

Where $i = 2, 3, ...n$

Then, to solve for $[\varphi]$, one has to solve Equation (3.14). Rewriting the equation in its matrix form gives,

$$
\overset{V}{\Downarrow}\begin{pmatrix} v_1 \\ \cdots \\ \cdots \\ v_{n-1} \\ v_n \end{pmatrix} = \overset{U}{\Downarrow}\begin{pmatrix} \alpha_1 & c_1 & & & \\ & \cdots & c_2 & 0 & \\ & & \cdots & \cdots & \\ & 0 & & \alpha_{n-1} & c_{n-1} \\ & & & & \alpha_n \end{pmatrix} \overset{\varphi}{\Downarrow}\begin{pmatrix} \varphi_1 \\ \cdots \\ \cdots \\ \varphi_{n-1} \\ \varphi_n \end{pmatrix} \tag{3.23}
$$

By backward substitution similar to the above procedure,

$$
\begin{aligned}
& v_n = \alpha_n \varphi_n \\
& \Rightarrow \boxed{\varphi_n = \frac{v_n}{\alpha_n}}
\end{aligned} \tag{3.24}
$$

Then based on this value of φ_n, one can obtain the entire $[\varphi]$ from,

$$
\begin{aligned}
& v_{n-1} = \alpha_{n-1}\varphi_{n-1} + c_{n-1}\varphi_n \\
& \varphi_{n-1} = \frac{v_{n-1} - c_{n-1}\varphi_n}{\alpha_{n-1}} \\
& \Rightarrow \boxed{\varphi_i = \frac{v_i - c_i \varphi_{i+1}}{\alpha_i}}
\end{aligned} \tag{3.25}
$$

Thus we have solved for $[\varphi]$ at each node point using this method

3.4. Successive Over Relaxation Method

We know that the finite difference approximation of the Poisson's equation is that mentioned in equation 3.10. Before we analyze the SOR method we must understand that every device has boundary conditions. There are three types of Boundary conditions:

Neumann: This a boundary condition on the derivative of the potential. This condition is applied at all imaginary boundaries of the device.

Dirichlet: This a boundary condition on the potential. This condition is applied at all node points in a device where the potential must be fixed (for example, contacts).

Mixed boundary condition: This is a mixture of Dirichlet and Neumann boundary conditions.

While applying boundary conditions on a particular structure, the device must have at least one node point where Dirichlet conditions have been enforced. The Dirichlet condition represents a connection to the real world. In other words, external voltage/bias will be applied at the node points where Dirichlet conditions have been enforced.

Consider the 1-D device in Fig 3.1. The figure indicates that there are two Dirichlet condition on the front and back end node points of the device which represent contacts. Neumann conditions are enforced in the middle.

Fig 3.1: Representation of Dirichlet and Neumann conditions on the node points of a device

Equation 3.10 can be viewed as

$$[A][\varphi] = [F]$$

(3.26)

where the 'A' matrix is the coefficient matrix, which in simple terms represents the effect that the surrounding node points have on 'i^{th}' node point and φ is the electrostatic potential at each node point. Consider Fig.3.2. The front and back end node points are Dirichlet contacts and the node points in the middle are internal nodes.

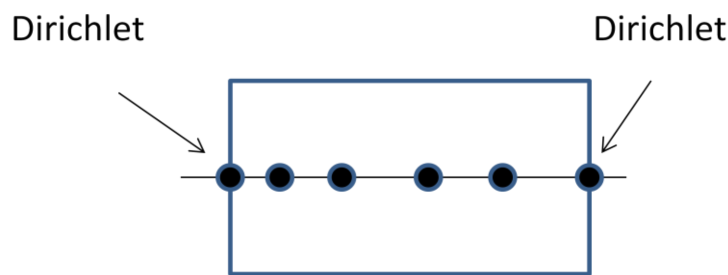

Fig 3.2: A hypothetical device with 6 node points.

$$\begin{pmatrix} 1 & 0 & . & 0 & . & 0 \\ a_1 & b_1 & c_1 & . & . & . \\ . & a_2 & b_2 & c_2 & . & . \\ . & . & a_3 & b_3 & c_3 & . \\ . & . & . & a_4 & b_4 & c_4 \\ 0 & . & 0 & . & 0 & 1 \end{pmatrix} \quad (3.27)$$

$$a_i = \frac{1}{\Delta^2}, b_i = \frac{2}{\Delta^2} + n_i + p_i, c_i = \frac{1}{\Delta^2}$$

(3.28)

Now let us describe the SOR method. The SOR method, is an extension of the Gauss-Seidel method. Both methods are iterative methods.

Iterative (or relaxation) methods start with an approximation (initial guess) which is successively improved by the repeated application (i.e. the "iteration") of the same algorithm, until a sufficient accuracy is obtained. In this way, the original approximation is "relaxed" toward the exact solution which is numerically more stable. Error analysis and convergence rate are two crucial aspects of the theory of iterative methods. We can define the residual as:

$$r^i = f - Av^i \tag{3.29}$$

where v^i is a sequence of approximations of x in Ax=f. The error between can be calculated as:

$$e^i = x - v^i \tag{3.30}$$

According to the Gauss-Seidel method the expansion of Ax=f is given by:

$$x_k^{i+1} = \frac{-\sum_{j=1}^{k-1} a_{kj} x_j^{i+1} - \sum_{j=k+1}^{n} a_{kj} x_j^i + f_k}{a_{kk}}; a_{kk} \neq 0 \tag{3.31}$$

By a simple modification of Gauss-Seidel's method it is often possible to improve the rate of convergence. By following the definition of a residual in equation 3.29, the Gauss-Seidel formula can be re-written as:

$$x_i^{k+1} = (1-\omega)x_i^k + \frac{\omega}{a_{ii}}(b_i - \sum_{j<i} a_{ij} x_j - \sum_{j>i} a_{ij} x_j^{k+1}) \tag{3.32}$$

Here, ω is the relaxation parameter. When ω=1, equation 3.32 will be reduced to equation 3.31. The relaxation parameter can be used to under damp or over damp the results. Successive over relaxation (SOR) leads to a surprisingly higher convergence than the Gauss-Seidel method.

3.5. Electron and Hole continuity Equation

The discretization of the continuity equation in conservation form requires the determination of the currents on the mid-points of mesh lines connecting neighboring grid nodes. Since the solutions are accessible only on the grid nodes, interpolation schemes are needed to determine the currents for consistency with Poisson's equation, it is common to assume that the potential varies linearly between two neighboring nodes. This is equivalent to assume a constant field along the mesh lines, and the field at the mid-point is obtained by centered finite differences of the potential values. In order to evaluate the current, it is also necessary to estimate the carrier density at the mid-points. The simplest approximation which comes to mind is to also assume a linear variation of the carrier density, by taking the arithmetic average between two neighboring nodes. This simple approach is only acceptable for very small potential variation between the nodes, and indeed is exact only if the field between two nodes is zero, which implies the same exact carrier density on the two points.

In order to illustrate this, let's consider a 1-D mesh where we want to discretize the electron current density:

$$J_n = q\mu_n n(-\frac{d\psi}{dx}) + qD_n \frac{dn}{dx} \tag{3.33}$$

Here, the field is explicitly expressed by the derivative of the potential. The discretization on the mid-point of the mesh line between nodes x_i and x_{i+1} is give by:

$$J_{i+1/2} = -q\mu_n n_{i+1/2} \frac{\psi_{i+1} - \psi_i}{\Delta x} + qD_n \frac{n_{i+1} - n_i}{\Delta x} \tag{3.34}$$

In the simple approach indicated above, the carrier density is expressed as:

$$n_{i+1/2} \approx \frac{n_{i+1} - n_i}{2} \qquad (3.35)$$

In equation 3.34, the assumed linearity of the potential between meshes, is implied by the use of the centered differences to express the field on the mid-point. We can now rewrite equation 3.34 including the approximation in equation 3.35 as:

$$J_{i+1/2} = n_{i+1}[-q\frac{\mu_n}{2}\frac{\psi_{i+1} - \psi_i}{\Delta x} + q\frac{D_n}{\Delta x}] - n_i[a+b] \qquad (3.36)$$

$$a = q\frac{\mu_n}{2}\frac{\psi_{i+1} - \psi_i}{\Delta x}, b = q\frac{D_n}{\Delta x} \qquad (3.37)$$

If we assume a condition where $J_n = 0$ (equilibrium) and a>>b (negligible diffusion), it is easy to see that positivity of the carrier density is not guaranteed, since the solution oscillates as $n_{i+1} \approx -n_i$. Also, it can be shown that for stability we need to have $\psi_{i+1} - \psi > \frac{2kT}{q}$, which requires very small mesh spacing.

The approach by Scharfetter and Gummel [13] has provided an optimal solution to this problem, although the mathematical properties of the proposed scheme have been fully recognized much later. They demonstrated that by allowing the electron density to follow an exponential variation between mesh points, errors due to discretization can be avoided.

Consider the 1-D electron current continuity equation under steady-state conditions:

$$\frac{1}{q}\nabla . J_n = G \tag{3.38}$$

which, by using the half point difference expansion based on the centered difference scheme gives:

$$\frac{1}{q}\frac{(J^n_{i+1/2} - J^n_{i-1/2})}{\Delta} = G_i \tag{3.39}$$

where,

$$J^n_{i+1/2} = qn\mu^n_{i+1/2}E_{i+1/2} + qD^n_{i+1/2}\frac{dn}{dx} \tag{3.40}$$

Equation 3.40 can also be written as:

$$\frac{dn}{dx} + \frac{\mu^n_{i+1/2}}{D^n_{i+1/2}}nE_{i+1/2} = \frac{J^n_{i+1/2}}{qD^n_{i+1/2}} \tag{3.41}$$

Writing the electric field in terms of potential we will obtain:

$$\frac{dn}{dx} - \frac{1}{V_T}n\frac{\psi_{i+1} - \psi_i}{\Delta} = \frac{J^n_{i+1/2}}{qD^n_{i+1/2}} \tag{3.42}$$

Equation can interpreted as the following:

$$\frac{dn}{dx} = \frac{dn}{d\psi}\frac{d\psi}{dx} = \frac{\psi_{i+1} - \psi_i}{\Delta}\frac{dn}{d\psi} \tag{3.43}$$

Equation 3.43 will lead to:

$$\frac{dn}{d\psi} - \frac{n}{V_T} = \frac{\Delta}{q(\psi_{i+1} - \psi_i)}\frac{J^n_{i+1/2}}{D^n_{i+1/2}} \tag{3.44}$$

Using Laplace transformation and the conditions $n(\psi_i) = n_i ; n(\psi_{i+1}) = n_{i+1}$,

we get:

$$n(\psi) = n_i[1 - g(\psi)] + n_{i+1} g(\psi) \tag{3.45}$$

where,

$$g(\psi) = \frac{\exp\frac{(\psi - \psi_i)}{V_T} - 1}{\exp\frac{(\psi_{i+1} - \psi_i)}{V_T} - 1} \tag{3.46}$$

where $g(\psi)$ is also known as the growth function.

Therefore, the electron current can now be given by:

$$J^n_{i+1/2} = \frac{qD^n_{i+1/2}}{\Delta}[n_{i+1}B(\frac{\psi_{i+1} - \psi_i}{V_T}) - n_i B(\frac{\psi_i - \psi_{i+1}}{V_T})] \tag{3.47}$$

where B is the Bernoulli function. This function is defined equation 3.52.

Similarly:

$$J^n_{i-1/2} = \frac{qD^n_{i-1/2}}{\Delta}[n_i B(\frac{\psi_i - \psi_{i+1}}{V_T}) - n_{i-1}B(\frac{\psi_{i-1} - \psi_i}{V_T})] \tag{3.48}$$

Therefore the final finite discretized system of equations for electrons and holes can be written as follows:

$$\frac{D^n_{i+1/2}}{\Delta^2} n_{i+1} B(\frac{\psi_{i+1} - \psi_i}{V_T}) - [\frac{D^n_{i-1/2}}{\Delta^2} B(\frac{\psi_{i+1} - \psi_i}{V_T}) + \frac{D^n_{i+1/2}}{\Delta^2} B(\frac{\psi_i - \psi_{i-1}}{V_T})] n_i$$
$$+ \frac{D^n_{i-1/2}}{\Delta^2} B(\frac{\psi_{i-1} - \psi_i}{V_T}) n_{i-1} = G_i$$

(3.49)

$$\frac{D^p_{i-1/2}}{\Delta^2} p_{i-1} B(\frac{\psi_i - \psi_{i-1}}{V_T}) - [\frac{D^p_{i-1/2}}{\Delta^2} B(\frac{\psi_{i-1} - \psi_i}{V_T}) + \frac{D^p_{i+1/2}}{\Delta^2} B(\frac{\psi_{i+1} - \psi_i}{V_T})] p_i$$
$$+ \frac{D^p_{i+1/2}}{\Delta^2} B(\frac{\psi_i - \psi_{i+1}}{V_T}) p_{i+1} = G_i \tag{3.50}$$

To speed up the computations, it is advantageous that the Bernoulli functions are evaluated using a set of predetermined values, i.e. approximations. This will eliminate the problem of overflows and underflows. Also the Sharfetter-Gummel scheme produced positive definite matrices and does not lead to coefficient matrices that have complex eigen values. Thus, even the SOR method can be used to solve this system of equations. All the half point values for the diffusion co-efficient and carrier mobilities can be obtained by linear interpolation.

$$D_{i+1/2} = \frac{D_i + D_{i+1}}{2}; \mu_{i+1/2} = \frac{\mu_i + \mu_{i+1/2}}{2} \tag{3.51}$$

The following is a useful scheme for the Bernoulli function:

$$B(x) = -x,\ x \le x_1$$
$$\frac{x}{e^x - 1},\ x_1 < x < x_2$$
$$1 - \frac{x}{2},\ x_2 \le x \le x_3$$
$$\frac{x\, e^{-x}}{1 - e^{-x}},\ x3 < x < x_4$$
$$x e^{-x},\ x_4 \le x < x_5$$
$$0,\ x \ge x_5 \tag{3.52}$$

3.6. Generation-Recombination Mechanisms

Non-equilibrium conditions prevail when the device is under the influence of an external voltage. In such situations there are various

generation/recombination events that take place which determine the characteristics of the device. In semiconductor physics the terms Recombination and generation can be defined as:

Recombination: A process in which an electron and hole are destroyed.

Generation: A process in which an electron and a hole are generated.

In this section we will discuss SRH, Radiative and Auger mechanisms.

3.2.2 *Shockley-Read-Hall Recombination*

Every semiconductor has trap levels that occur in the energy bandgap. These intermediate levels can be defect induced or impurity induced. These trap levels function as 'recombination-generation' centers (r-g centers). In many semiconductors recombination/generation often occurs through these centers and is known as SRH recombination events. In indirect bandgap materials such as silicon, the SRH process is more dominant when compared to $Hg_xCd_{1-x}Te$ which in comparison is a direct bandgap material. The recombination and generation that occur through r-g centers are characterized by a set of emission and capture processes. This is illustrated by fig 3.3.

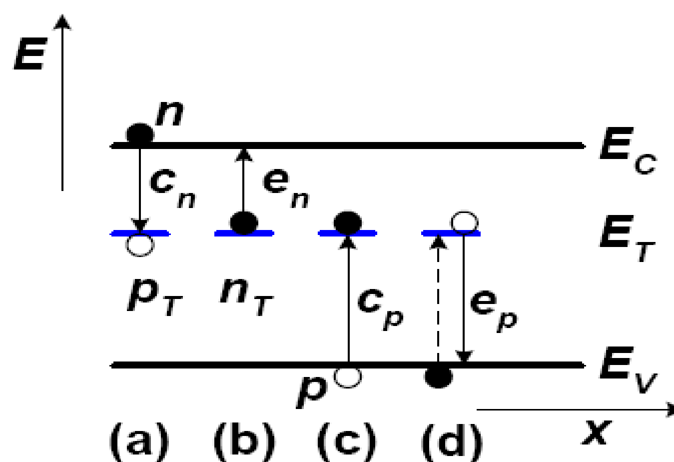

Fig 3.3: All permutations of emission and capture events. (Courtesy Dr. Schroder)

The capture events are represented by c_n (electron capture) and c_p (hole capture). The emission events are represented by e_n (electron emission) and e_p (hole emission). Situation (a) and (c) represent a recombination event. In (a), an electron falls from the conduction band into a trap filled with a hole to recombine with a hole, whereas in (b) a hole rises into a trap filled with an electron to recombine. (b) and (d) represent emission processes. In (b) a trap filled with an electron releases the electron into the conduction band, which can be interpreted as a generation event. Event (d) can be interpreted in two ways. It can either be looked upon as a hole being released in to the valence band or an electron being captured from the valence band, which is indirectly the generation of a hole.

The conventional SRH net recombination rate is given by:

$$R_{SRH} = \frac{pn - n_i^2}{\tau_p(n + n_i \exp\frac{E_t - E_i}{kT}) + \tau_n(p + n_i \exp\frac{-E_t + E_i}{kT})} \tag{3.53}$$

where , E_t is the trap level, E_i is the intrinsic energy level and $\tau_n$and τ_p are the electron and hole lifetimes. These lifetimes are heavily dependent on the concentration of the trap centers. The SRH lifetimes are given by:

$$\tau_n = \frac{1}{\sigma_n V_{th} N_T}; \tau_p = \frac{1}{\sigma_p V_{th} N_T} \tag{3.54}$$

where $\sigma_{n,p}$is the capture cross section for electron and holes respectively, V_{th} is the thermal velocity and N_T is the trap concentration. V_{th} is also said to be average speed due to “Brownian-Like” motion or random motion at a given temperature [14]. V_{th} is given by the following equation:

$$V_{th} = \sqrt{\frac{3kT}{m_{n,p}^{*}}} \tag{3.55}$$

The $\sigma_{n,p} \times N_T$ values do depend heavily upon the purity of the growth technique. Work done in relation to SRH lifetimes in $Hg_{1-x}Cd_xTe$ in Ref [15] is provides certain values of trap concentrations.

It is a well known fact that in the presence of strong electric fields, tunneling of electrons can make a significant contribution to carrier transport in a p-n junction. Band to band tunneling as well as trap assisted tunneling can become dominant factors that determine the current. Tunnelling not only adversely affects the leakage currents but it can also lead to an anomalously high non-ideal currents under forward bias. In the context of a highly doped narrow bandgap semiconductor like $Hg_xCd_{1-x}Te$, tunnelling can play a pivotal role due to the large electric fields that will be generated in the space charge region. Moreover, in a highly doped junction the tunnelling distances are short, making the effect quite significant. The emission of electrons and holes can also be enhanced by phonon assisted transitions [16]. Instead of thermal emission over the entire trap depth (which is the only possibility in the absence of an electric field), carriers can also be emitted by thermal excitation over only a part of the trap depth and followed by tunnelling through the rest of the potential barrier.

Trap assisted tunnelling can be implemented by adding a term to the SRH recombination term as done in [17]. The SRH equation with trap assisted tunnelling is given by:

$$R_{SRH} = \frac{pn - n_i^2}{\frac{\tau_p}{1+\Gamma_p}[n + n_i \exp(\frac{E_T - E_i}{kT})] + \frac{\tau_n}{1+\Gamma_n}[p + n_i \exp(\frac{E_i - E_T}{kT})]}$$

(3.56)

In equation 3.56, two new terms, namely Γ_n and Γ_p are introduced. They are the field effect functions. In cases of weak electric fields $\Gamma_{n,p} \ll 1$, equation 3.56 reduces to the conventional SRH recombination term.

The expression for $\Gamma_{n,p}$is given by the following expression:

$$\Gamma_{n,p} = \frac{\Delta E_{n,p}}{kT} \int_0^1 \exp[\frac{\Delta E_{n,p}}{kT} u - K_{n,p} u^{3/2} du \qquad (3.58)$$

$K_{n,p}$ is given by equation (3.59)

$$K_{n,p} = \frac{8\pi}{3} \frac{\sqrt{2m^* \Delta E_{n,p}^3}}{qh|F|} \qquad (3.59)$$

ΔE_n and $\Delta E_p$are given by the following expression:

$$\begin{aligned} \Delta E_n(x) &= E_c(x) - E_{cn}, E_T(x) \le E_{cx} \\ \Delta E_n(x) &= E_c(x) - E_T(x), E_T(x) > E_{cx} \\ \Delta E_p(x) &= E_{vp}(x) - E_v(x), E_T(x) > E_{vp} \\ \Delta E_p(x) &= E_T(x) - E_v(x), E_T(x) \le E_{vp} \end{aligned} \qquad (3.60)$$

where $E_c(x)$ and $E_v(x)$ are the spatially varying conduction and valence band energies. E_{cn} and E_{vp} are the equilibrium values of the conduction and valence band energies.

Analytical expressions for the integral in equation 3.58 are given as follows.

For $K_{n,p} > \frac{2}{3}\frac{\Delta E_{n,p}}{kT}$

$$\Gamma_{n,p} = 2\sqrt{3\pi}\frac{|F|}{F_{\Gamma}}\exp\left(\frac{F}{F_{\Gamma}}\right)^{2} \tag{3.61a}$$

where F is the local electric field and F_{Γ} is given by:

$$F_{\Gamma} = \frac{2\pi\sqrt{24m^{*}(kT)^{3}}}{qh} \tag{3.61b}$$

For $K_{n,p} < \frac{2}{3}\frac{\Delta E_{n,p}}{kT}$

$$\Gamma_{n,p} = \frac{\Delta E_{n,p}}{kT}\sqrt{\frac{2\pi}{3K_{n,p}}}(a_1 t_{n,p} + a_2 t_{n,p}^{2} + a_3 t_{n,p}^{3})\exp\left(\frac{\Delta E_{n,p}}{kT} - K_{n,p}\right) \tag{3.62a}$$

Here $t_{n,p}$ is given by:

$$t_{n,p} = \left[1 + \beta\frac{\frac{\Delta E_{n,p}}{kT} - \frac{3}{2}K_{n,p}}{\sqrt{\frac{3}{2}K_{n,p}}}\right] \tag{3.62b}$$

In equation 3.62b β = 0.61685, a_1 = 0.3480242, a_2 = -0.0948798, and a_3 = 0.7478556.

3.2.3 *Radiative Recombination*

This is a band to band type of recombination which involves the direct annihilation of a conduction band electron with a valence band hole. The electron falls from an allowed conduction band state in to a vacant valence band state. The excess energy produced is usually released in the form of a

photon. This mechanism is more prominent in a direct bandgap material. Radiative recombination is given by the expression:

$$R_{Radiative} = B(pn - n_i^2) \tag{3.63}$$

B is given by the expression in equation 3.64.

$$B = (5.8\times10^{-13})\varepsilon^{1/2}\left(\frac{m_0}{m_e^* + m_h^*}\right)\left(1 + \frac{m_0}{m_e^*} + \frac{m_0}{m_h^*}\right)\left(\frac{300}{T}\right)^{3/2}\left(E_g^{\ 2} + 3kTE_g + 3.75k^2T^2\right) \tag{3.64}$$

As $Hg_{1-x}Cd_xTe$ is a direct bandgap semiconductor, we may expect Radiative recombination to play quite a prominent role. However, that is not true. For narrow bandgap $Hg_xCd_{1-x}Te$ with x=0.225, Radiative recombination does not dominate across all temperature ranges. In fact, SRH mechanism remains more prominent than Radiative in narrow bangap materials. However, in wide bandgap HgCdTe with x=0.31, Radiative recombination remains prominent at all temperatures [18].

3.2.4 *Auger Recombination*

Auger Recombination mechanisms is one of the dominat mechanisms in narrow bandgap HgCdTe. Auger generation typically dominates the dark current at elevated temperatures, where the low doped absorber layer becomes intrinsic and the carrier concentration is higher than the doping level. Standard p–n junction photodiodes therefore become very noisy when operated near room temperature. This is the prime reason why HgCdTe photodiodes are operated near liquid nitrogen temperatures, even though operating at such low

temperatures increases the operating cost tremendously. Different designs are often implemented to suppress Auger generation.

There are reportedly many types of Auger mechanisms that occur in HgCdTe, but the only ones of consequence are Auger-1 and Auger-7 mechanisms. Auger-1 (τ_{A1}) is the dominant mechanism in n-type HgCdTe. In this mechanism an excited electron in the conduction band recombines with a hole in the valence band and the loss in energy is transferred to a second conduction band electron. Auger-7(τ_{A7}) mechanism is predominant in p-type HgCdTe. The energy in this case is transferred to an electron in the light hole band. The lifetimes for Auger-1 and Auger-7 are given by the following expressions.

$$\tau_{A1} = \frac{2n_i^2 \tau_{A1}^i}{(p+n)} \tag{3.65a}$$

$$\tau_{A7} = \frac{n_i^2 \gamma \tau_{A1}}{(p+n)p} \tag{3.65b}$$

The intrinsic Auger lifetime is given by the expression:

$$\tau_A^i = \frac{3.8 \times 10^{-18} \varepsilon^2 (1+\eta)^{1/2} (1+\eta)}{\left(\frac{m_e^*}{m_0}\right) |F_1 F_2|^2 \left(\frac{kT}{E_g}\right)^{3/2}} \exp\left[\frac{(1+2\eta)}{(1+\eta)} \frac{E_g}{kT}\right] \tag{3.65c}$$

where $\eta = \frac{m_e^*}{m_h^*}$. $|F_1 F_2|$ is the overlap integral which usually lies between 0.1 to 0.3 and m_e^* and m_h^* are the effective electron and hole masses.

The recombination-generation term for Auger mechanisms is given by equation 3.66.

$$R_{Auger} = C_n(pn^2 - nn_i^2) + C_p(np^2 - pn_i^2) \qquad (3.66)$$

C_n and C_p are the Auger coefficients. They are given by the following expression which can also be found in Ref [19]. In Fig 3.4 we show two curves of Auger lifetimes plotted vs. 1000/T for different doping densities. We notice that, as the temperature increases, the lifetime increases but after we reach room temperatures, the lifetime sharply decreases.

3.2.5 *Optical Generation*

When a radiation is incident upon a device, EHP's are generation if the radiation has sufficient energy to excite electrons from the valence band into the conduction band. If the radiation does not have sufficient energy, the device will be transparent to the radiation. The generation EHP's are

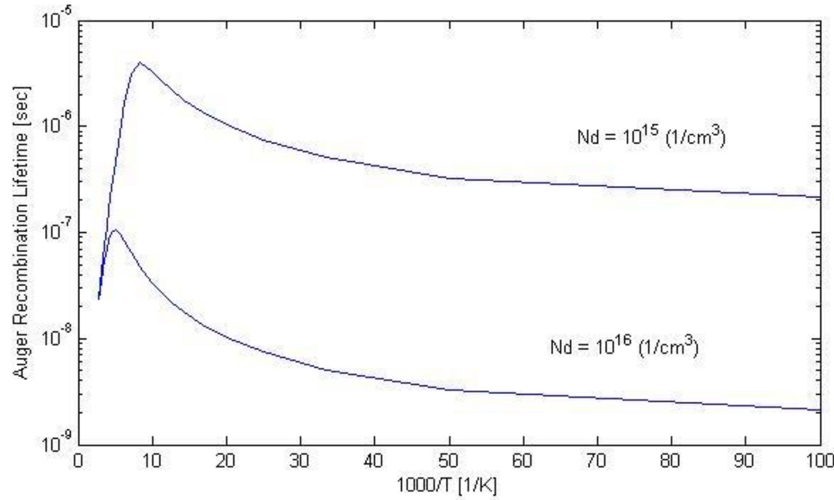

Fig 3.4: Auger Lifetimes vs. 1000/T for different doping densities.

represented by generation term. This generation term depends heavily on the kind of absorption that occurs in the device. All materials have a unique

absorption spectrum related to them. The generation term is given by the expression:

$$G(x) = \frac{a(\lambda)(1-R)P_{OPT}}{Ahv} \exp\left[-a(\lambda)x\right] \tag{3.67}$$

As is evident from the above expression, radiations with different wavelengths will result in different amounts of generation throughout the device. The generation for each wavelength is calculated at every node point in the device except at the contacts. This term is then added to the generation recombination term alongside all the recombination mechanisms discussed earlier.

3.7. Optical Absorption Model

The absorption coefficient is characterized by the intrinsic Kane Region which is valid for energies above the conduction band edge and the Urbach model [20] which describes the absorption coefficient for energies below the conduction band edge. It is well known that the Kane region represents optical transitions of electrons from the valence band to the conduction band; in other words the Kane region is due to direct band to band transitions. It is also well known that absorption takes place for radiation which have energies lesser than the band gap and this type of absorption is described by the Urbach tail. This happens due to a number of different interactions such as, electron-phonon, electron-impurity and electron interactions with intermediate trap states which are generated by defects in the material. Both regions have been investigated thoroughly and large amounts of empirical data already exist [21].

According to the Urbach model (valid below the conduction band edge) the absorption coefficient obeys an exponential law whereas for the Kane region a square root law relates α and energy (E). Therefore:

For the Kane region:

$$\alpha = \beta\sqrt{E - E_g}$$
$$\beta = -1 + 0.083T + (21 - 0.13T)x \qquad (3.68)$$

For the Urbach region:

$$\alpha = \alpha_0 \exp\left(\frac{E - E_0}{T + T_0}\right)$$
$$\alpha_0 = 3.267 \times 10^4 (1 + x)$$
$$E_0 = (1.838x) - 0.3424$$
$$T_0 = 81.9 \qquad (3.69)$$

The absorption coefficient also plays a pivotal role in determining the Quantum Efficiency which will be discussed in the next chapter. In Fig 3.5 we can see the Absorption coefficient for different mole concentrations (*x=0.225,0.3,0.4)* vs. energy.

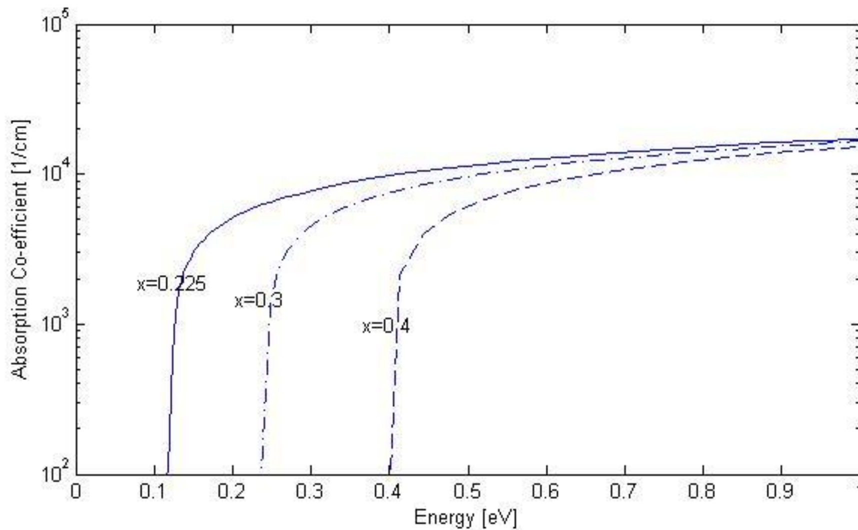

Fig 3.5: Absorption Coefficient vs. Energy for $Hg_x Cd_{1-x}Te$ for x=0.225, 0.3 and 0.4.

3.8. Flowchart of the simulation program

This section describes the simulation methodology adopted by the tool 'OPTODET'. Fig 3.5 is a flowchart of the simulation program. 'OPTODET' is a drift diffusion based simulator. There are two sections that the tool is divided into. One section focuses on the I-V characteristics (dark current, dynamic resistance, etc.) whereas the other section calculates the optical solutions. The optical based solutions include results such as Quantum Efficiency, Responsivity, Detectivity, Absorption Coefficient etc. While the I-V characteristics section can calculate current under the influence of illumination, it considers the total generation by the given spectrum. The optical solutions section will calculate current for every individual wavelength.

As this tool is also supposed to serve an educational purpose, great flexibility has been provided in terms varying the mesh size, voltage increments and specific models the user would like to use. By providing this functionality the user can observe the effect of every phenomenon singularly. For example, the user can selectively switch "off" the tunneling effect and see the dark current characteristics without the effects of tunneling. Similarly, the user can select between SRH, Radiative and Auger recombination mechanisms. Observing the results in this way will lead to a better understanding of which mechanisms dominant under different conditions. .

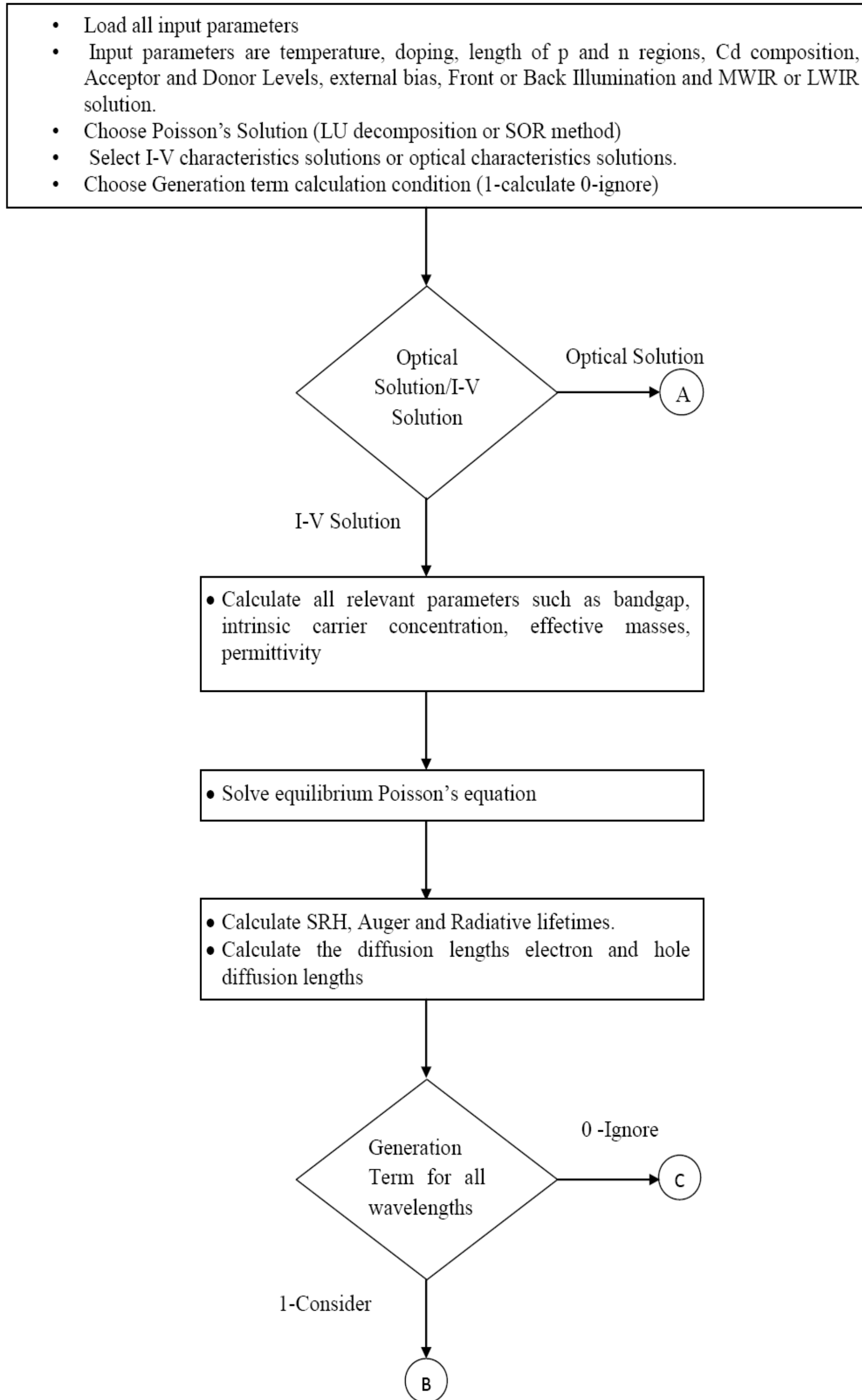

Fig 3.6 (a): Flowchart of simulation program.

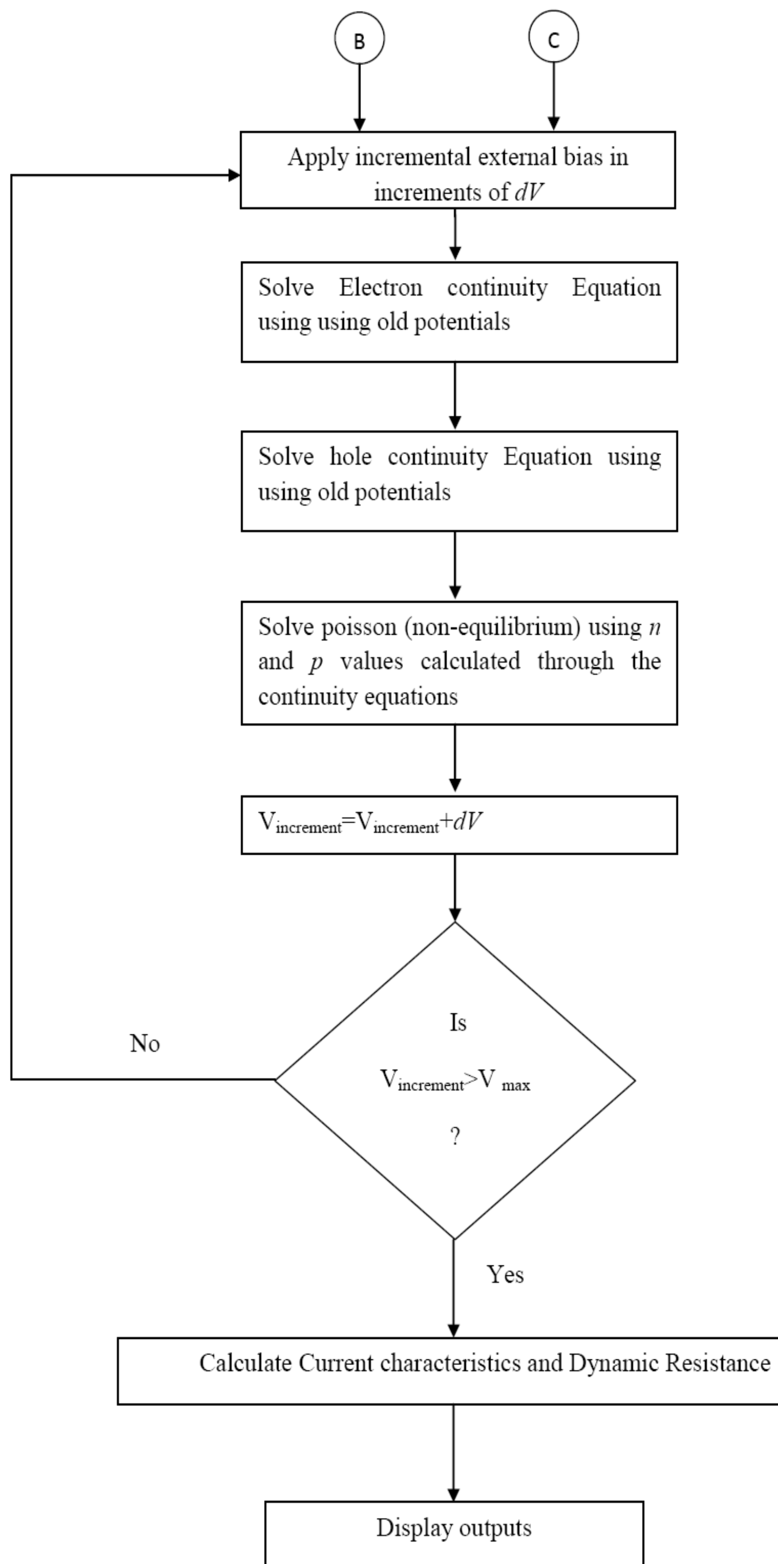

Fig 3.6 (b): continuation of flow chart.

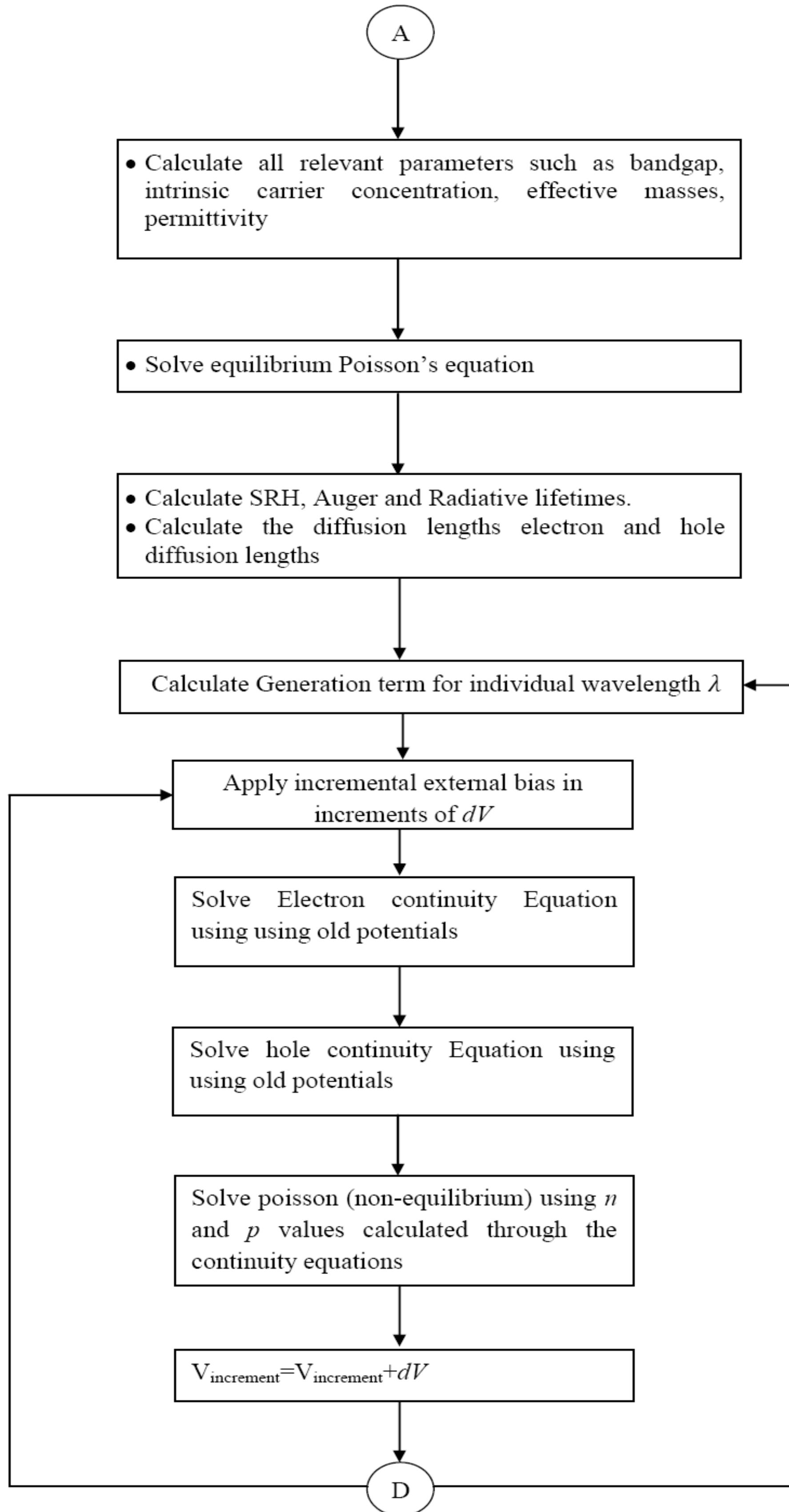

Fig 3.6 (c): continuation of flowchart.

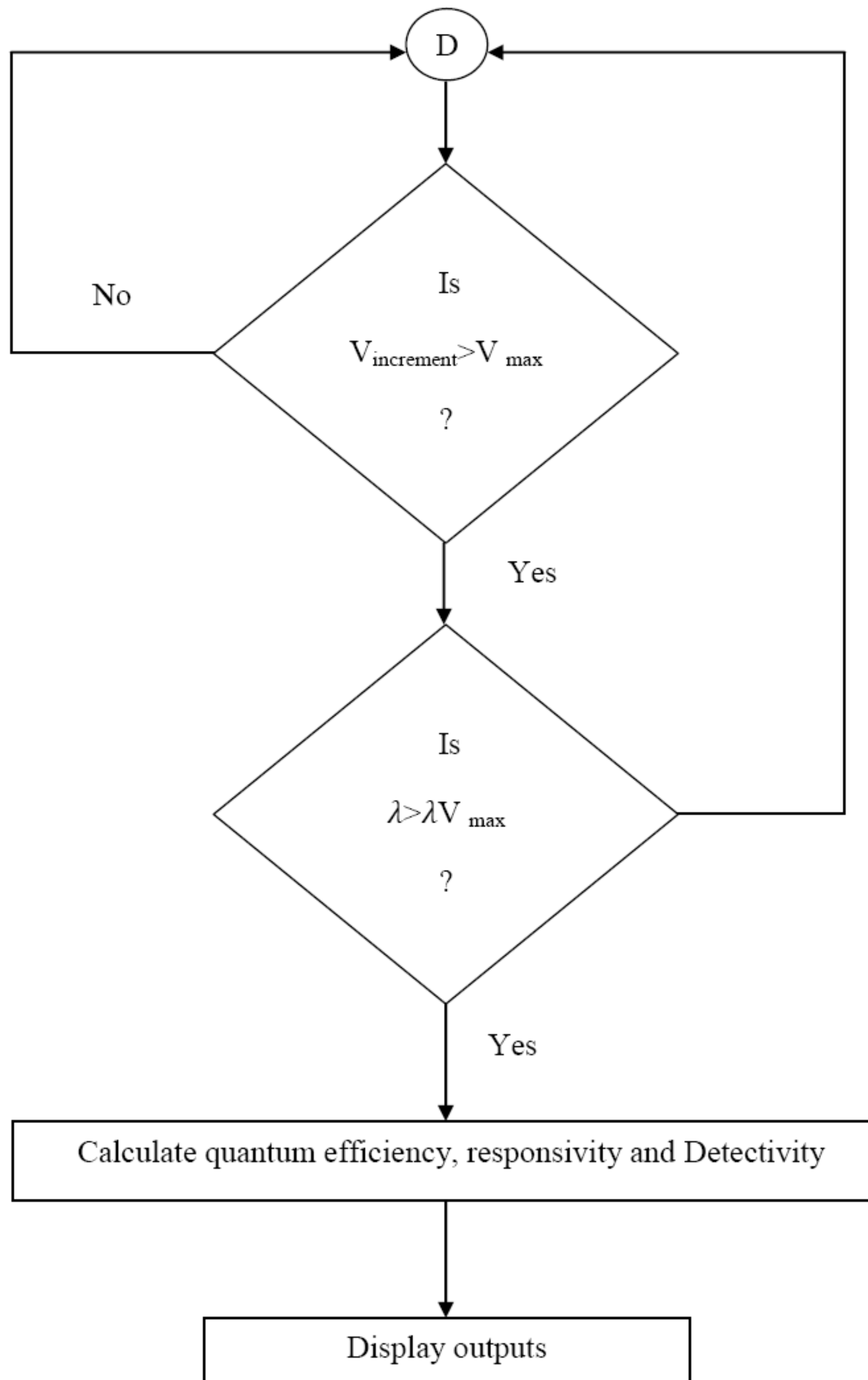

Fig 3.6 (d): Continuation of flow chart.

MODELING OF HgCdTe PHOTODETECTORS

Among the narrow band-gap semiconductors, $Hg_{1-x}Cd_x$ Te has taken a leading role as a source material for intrinsic infrared detectors. The two compositions which are specifically of use are *x-0.2* and *x-0.3,* which correspond to the two atmospheric spectral windows of 8-12 and 3-5 μm. HgCdTe is a direct bandgap semiconductor with a zinc blende structure. As already mentioned in previous sections, the material properties of $Hg_{1-x}Cd_xTe$ are very sensitive to the mole concentration *x* and temperature. There are several properties that make mercury cadmium telluride an attractive choice as an optical detector in the infrared region. We will elaborate on these properties below.

4.1. Material Properties

4.1.1 *Intrinsic Carrier Concentration*

The intrinsic carrier concentration is given by:

$$n_i = (5.585 - 3.820x + 1.753\times10^{-3}T - 1.364\times10^{-3}xT)\times10^{14}E_g^{3/4}T^{3/2}\exp\left(-\frac{E_g}{2kT}\right)cm^{-3} \tag{4.1}$$

Where *'x'* is the cadmium mole fraction, T is the temperature and E_g is the bandgap. As we can see the intrinsic carrier concentration (n_i) does depend on the mole fraction as well as the temperature. This equation is valid for $x \leq 0.7$ and $50K \leq T \leq 300K$ .In Fig.4.1 we can see the dependence of n_i on

temperature at $x=0.225$ and Fig.4.2 depicts the relation between n_i and the mole concentration at T=78 K.

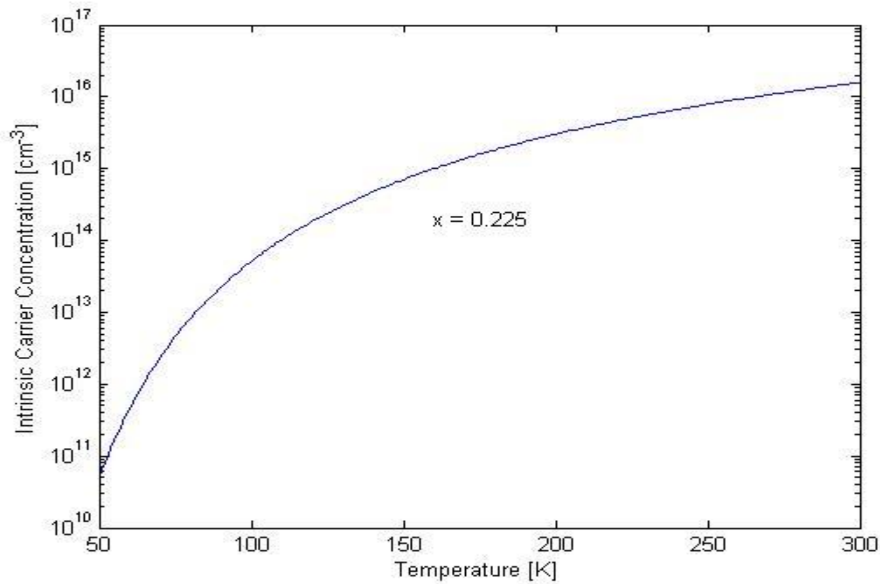

Fig 4.1: Intrinsic Carrier Concentration vs. Temperature.

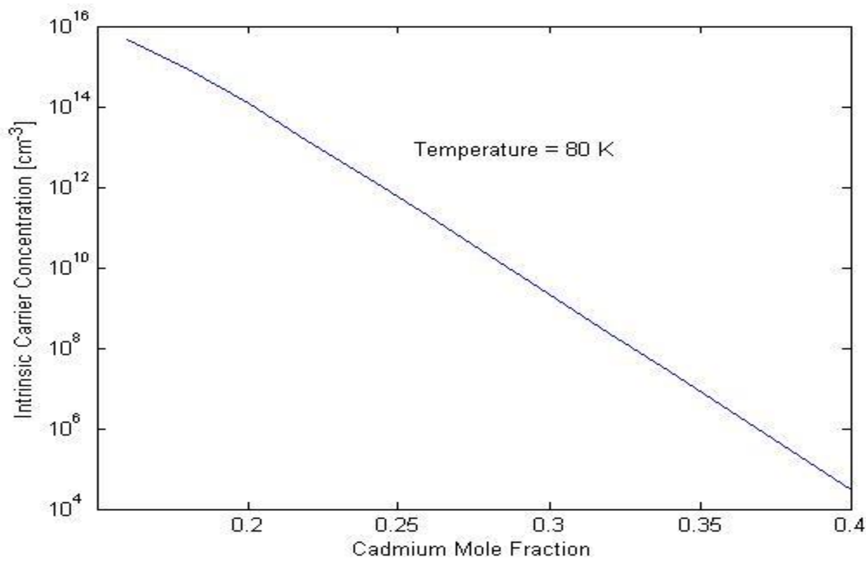

Fig 4.2: Intrinsic Carrier Concentration vs. Cadmium Mole Fraction (x).

Fig.4.3 shows the variation of intrinsic carrier concentration with change in mole fraction at different temperatures.

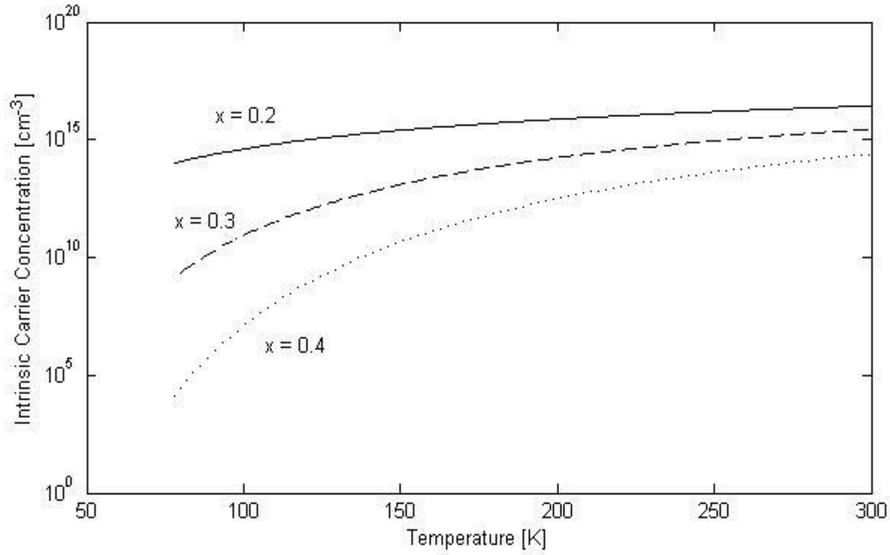

Fig 4.3: Intrinsic Carrier Concentration vs. Mole fraction at 78 K, 100 K, 150 K, 250 K and 300 K.

We can clearly see that at lower temperatures the intrinsic carrier concentration seems to be more sensitive to change in the cadmium concentration.

4.1.2 *Bandgap*

The expression for the bandgap is given by:

$$E_{(x,T)} = -0.302 + 1.93x + 5.35\times10^{-4}T(1-2x) - 0.810x^2 + 0.832x^3 \quad (4.2)$$

where, ‘ x’ is the cadmium mole fraction and T is the temperature. It is a well known fact that the bandgap of HgCdTe can be tuned by changing the mole fraction. The temperature too plays a role in changing the bandgap. The fact that the bandgap can be changed allows us to access the narrow bandgap properties and the wide bandgap properties that the material can offer. Fig.4.4 shows how the bangap varies will the mole fraction.

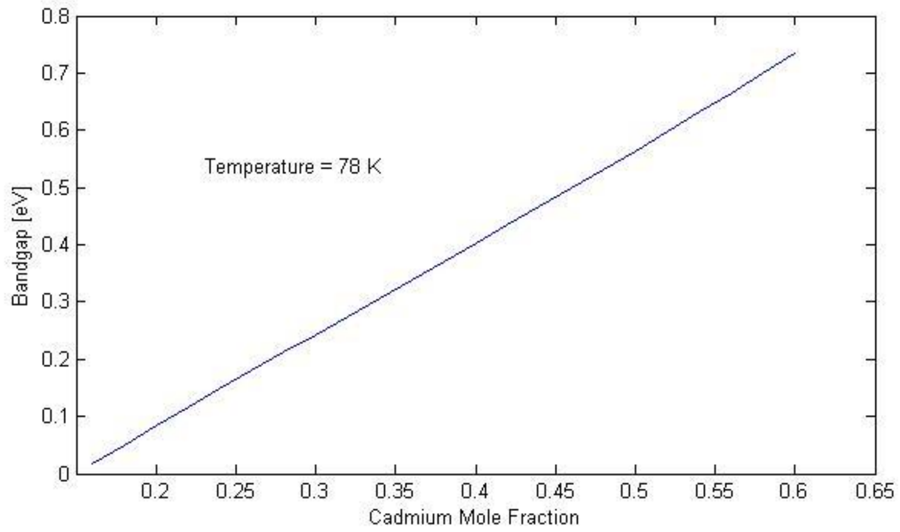

Fig 4.4: Bandgap vs. Mole Fraction at 78 K.

Equation 4.2 is valid for $0 \leq x \leq 0.6$ and 4.2K $\leq$ T $\leq$ 300 K [22]. Fig.4.5 shows the variation of the bandgap with temperature at a certain mole fraction. The bandgap increases with the increase in temperature. This fact becomes significant when we analyze the behaviour of the device at different temperatures.

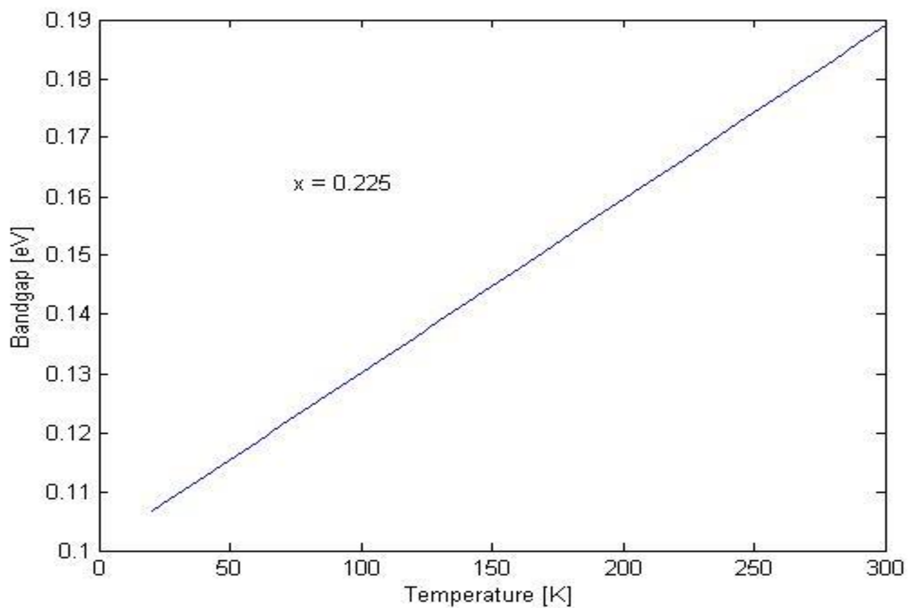

Fig 4.5: Bandgap vs. Temperature at x=0.225.

4.1.2 *Effective Masses*

The electron effective mass is given by:

$$m_n^* = \frac{1}{-0.6 + 6.333\left(\dfrac{2}{E_g} + \dfrac{1}{E_g + 1}\right)} \qquad (4.3)$$

where, E_g is the bandgap. The hole mass m_p^* is given as $0.55m_o$. HgCdTe is characterized by very low electron effective mass when compared to the hole effective mass. This in many ways shapes the way the device behaves. Since the electron mass is so low, the electrons also tend to have a very high mobility when compared to the holes. This property can be used to make a high performance detector. Detectors are designed in such a way that the electrons carry the majority of the current. This also results in better transit times.

4.1.4 *Mobility*

The expression for mobility is :

$$\mu_e = 9 \times 10^4 \left(\frac{0.2}{x}\right)^{7.5} T^{-2\left(\frac{0.2}{x}\right)^{0.6}} \qquad (4.4)$$

Where x is the mole fraction and T is the temperature. The hole mobility is usually given by:

$$\mu_h = \frac{\mu_e}{100} \qquad (4.5)$$

HgCdTe has very high electron mobility. There are various scattering mechanisms that would affect the mobility as we increase temperature but that will not be discussed in this thesis. In HgCdTe the theoretically calculated mobility is usually greater than the experimental value at low temperature. It is

because sufficient information is not represented for theoretical calculation especially concerning impurity level, compensation, and impurity iconicity [23].

4.1.5 *Permittivity*

The expression for permittivity is given by:

$$\varepsilon_{HgCdTe} = 20.5 - 15.5x + 5.7x^2 \tag{4.6}$$

4.2. Simulation Characteristics

In this section we will discuss the simulated results.

4.2.1 *I-V Characteristics*

In an Ideal diode, we can say that the photodiode current is limited by diffusion. But in a narrow bandgap pn junction such as $Hg_{1-x}Cd_xTe$ this is usually not the case. Several additional mechanisms play significant roles in determining the dark current characteristics of the photodiode. The dark current is the cumulative current contributed by three regions: the bulk, the space charge region and the surface [24].

- *Thermally generated current in the bulk and depletion region*:

i) Diffusion current in the bulk and p and n regions.

ii) Generation – Recombination current in the depletion region.

iii) Band to Band tunnelling.

iv) Trap assisted tunnelling.

v) Anomalous Avalanche current.

vi) Ohmic Leakage across the depletion region.

- *Surface leakage current*:

i) Surface generation current from surface states.

ii) Generation current in a field induced surface depletion region.

iii) Tunnelling induced near the surface.

iv) Ohmic or non-Ohmic shunt leakage.

v) Avalanche Multiplication in a field-induced surface region.

While all these mechanisms may not take place together, all these mechanisms become significant if the conditions are appropriate. In this thesis work we have not incorporated the effects of surface leakage current.

In an ideal diode which is diffusion limited we know that after a certain reverse voltage the reverse current is independent of the voltage. But in a HgCdTe device several other mechanisms become relevant at low temperatures. The main one that we have considered is tunnelling. The tool 'OPTODET' has implemented both trap assisted tunnelling (discussed in chapter 3), and band to band tunnelling. In fig 4.6 we can see the diffusion region and tunnelling dominated regions of the dark current.

We have added a tunneling model based on the WKB approximation [25]. For a 1-D case, the generation term due to tunneling is given by:

$$G_T(x) = \frac{\sqrt{2}q^2\sqrt{m^*}F_x^2}{4\pi^2\hbar\sqrt{E_g}}\exp\left[\frac{-\pi\sqrt{m^*}E_g^{3/2}}{2\sqrt{2}q\hbar F_x}\right]\left(cm^3\sec^{-1}\right) \qquad (4.7)$$

Tunneling probability strongly depends on the shape of the potential barrier. Also, usual direct tunneling calculations assume constant effective mass over

the potential barrier. Expression (4.7) was obtained for a parabolic

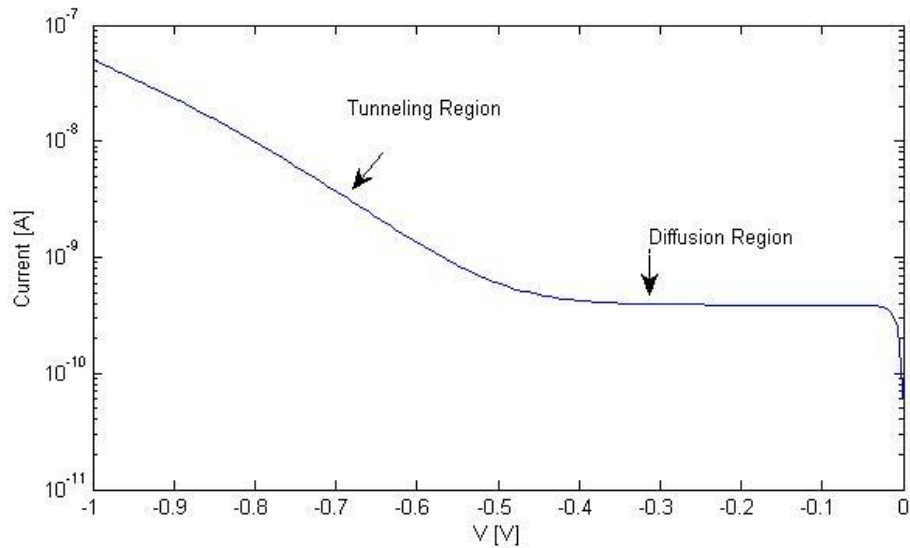

Fig 4.6: Dark Current Characteristics with Diffusion Region and Tunneling region.

barrier [see Ref 25]. While the advantage offered by the WKB expression in equation 4.7 is that can easily be integrated into the generation term of the continuity equation. The disadvantage however is that while this model serves the purpose during low field conditions, but when the device is under very large bias, the WKB expression will give erroneous results.

Fig.4.7 shows the dark current characteristics for 3 different temperatures. We can clearly see that the I-V curve at 100 K looks more like the current characteristics of a diffusion limited diode. This behavior occurs at higher temperatures due to the increase in bandgap, and therefore, tunneling is not as relevant. Similarly we notice that at lower temperatures, the tunneling dominated part of the curve occurs at a lower bias as the bandgap is lesser at those temperatures.

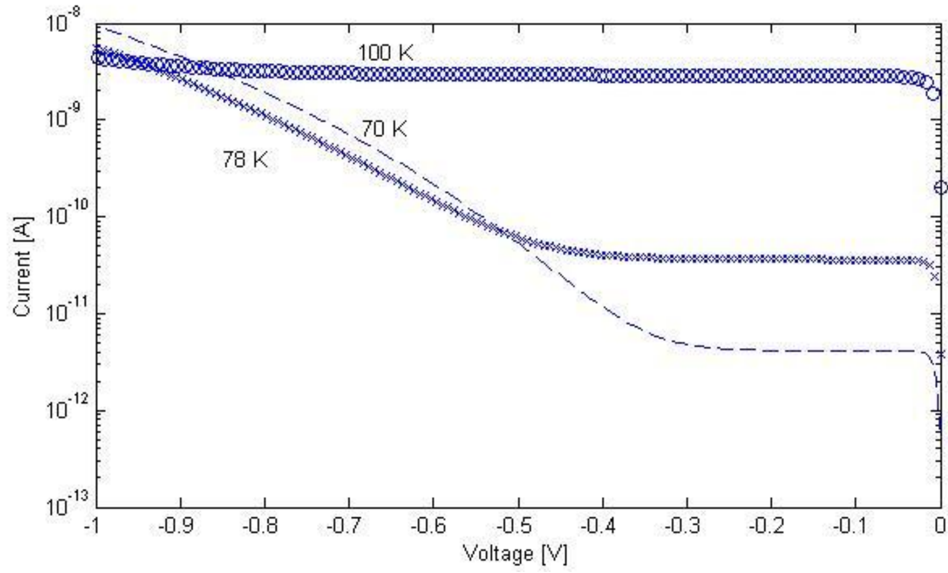

Fig 4.7: Dark Current Characteristics for $Hg_{1-x}Cd_xTe$ with x=0.225. p^+-n junction with $N_a = 2\times10^{16}$ cm^{-3} and $N_d = 10^{15}$ cm^{-3}.

In Fig.4.8 we can see the dark current characteristics with and without the tunneling model.

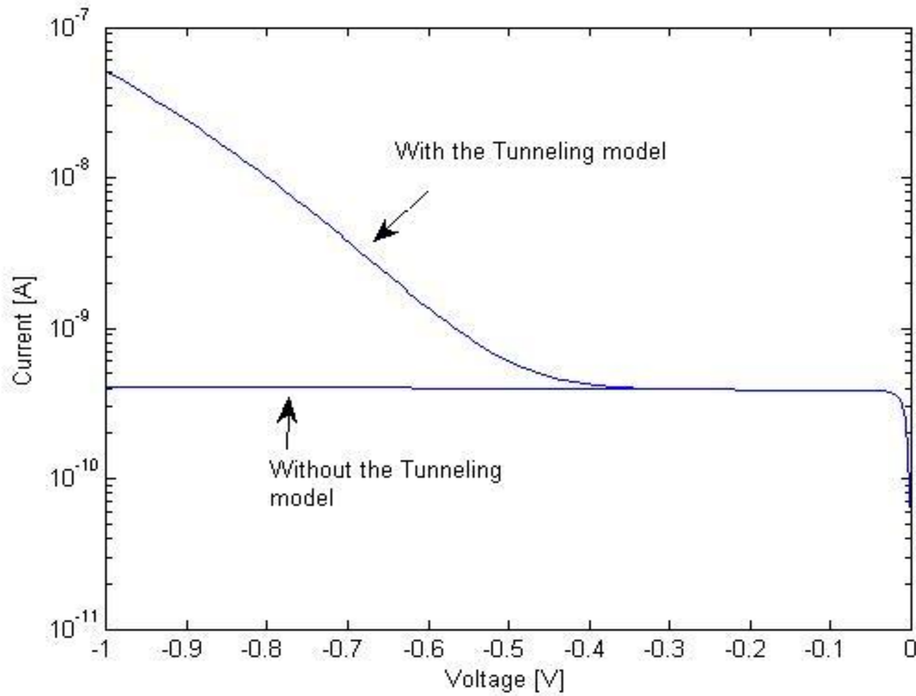

Fig 4.8:Dark current with and without the tunneling models.

Another point to note is that, direct tunneling is critically dependent on the electric field; this however, is not the case with trap assisted tunneling. The different role played by the two types of holes should be noted. Since the tunneling rate of carriers is inversely proportional to the exponent of their mass, the tunneling probability of heavy holes is much smaller than light holes. But since the density of states of the heavy holes is more, the heavy holes dominate the thermal transitions. Trap assisted tunneling increases exponentially with decreasing effective mass, thus the light holes dominate that transition. The density of recombination centers and their position in the bandgap is also a significant factor that determines the trap assisted tunneling. The maximum tunneling probability arises for mid gap states [26].

4.2.2 *Dynamic Resistance*

The dynamic resistance is the incremental resistance that is measured. It is given by the expression:

$$R_{Dynamic} = \left(\frac{dI}{dV} \right)^{-1} \quad (4.8)$$

This is an important parameter as it plays a major part in determining various other parameters such as detectivity and responsivity. The dynamic resistance also determines the R_0A product. R_0 being the zero bias resistance. The dynamic resistance for the same parameters as those from Fig.4.7 is shown in Fig.4.9. For x=0.225 at 78 K we obtained $R_0A = 15\Omega cm^{-2}$. This value can even be extracted from the Fig.4.9 at $(\frac{dI}{dV})^{-1}$ at V=0. A larger R_0A value will lead to a higher detectivity. At 60-70 K the R_0A values $\approx 10^2 - 10^3\ \Omega cm^{-2}$.

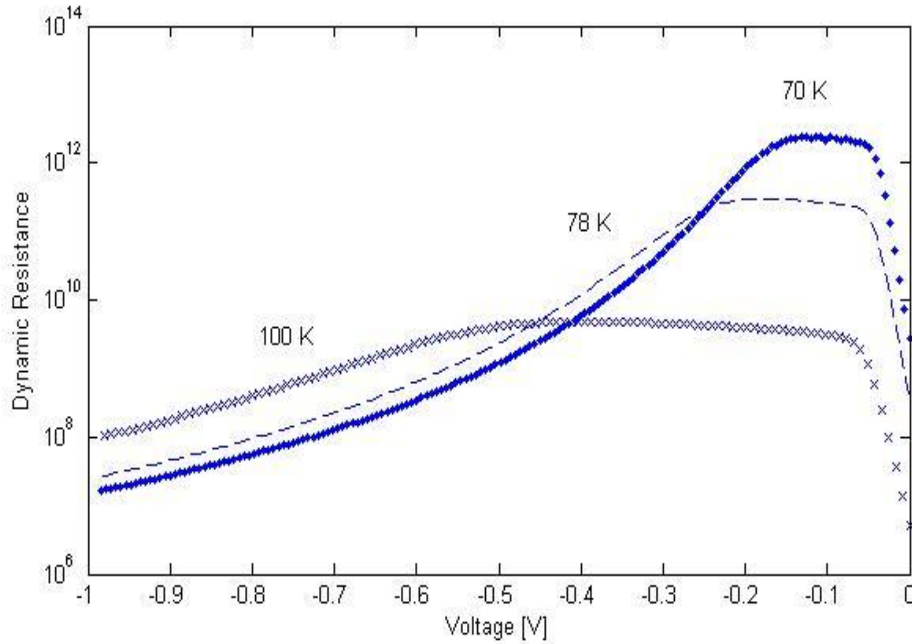

Fig 4.9: Dynamic resistance vs Reverse Voltage

4.3. NEP

The principal issue usually facing the system designer is whether the system will have sufficient sensitivity to detect the optical signal which is of interest. One figure of merit that answers that question is Detectivity. We have already defined detectivity in chapetr 2. Another way of looking at detectivity is given by the following expression:

$$D^* = \frac{\sqrt{A \times \Delta f}}{NEP} \tag{4.9}$$

where 'A' is the area in cm^2, Δf is the bandwidth in Hertz and NEP is the noise equivalent power.

The initial concept is to define the noise equivalent power as the optical power which will yield a signal to noise ratio of 1. This is then the limit of what can be detected. But with this definition the noise equivalent power can only be given at a specific bandwidth (Δf enters in the expression of

S/N).NEP is also defined the minimum detectable power per square root of bandwidth. Therefore now the NEP can be given by the expression:

$$NEP = \frac{\sqrt{A \times \Delta f}}{D^*} \tag{4.10}$$

For a 10 micron p^+-n device for x=0.225, the bandwidth is a few terahertz, the detectivity ≈ 10^{11} Jones. The NEP obtained is ≈ 10^{-8}-10^{-9}. The units of NEP are $\frac{W}{\sqrt{Hz}}$.

4.4. Detectivity

In chapter 2 we introduced and outlined the concept of detectivity. We also mentioned the conditions for background limited performance. In Fig.4.10 the detectivity for a LWIR $Hg_{1-x}Cd_xTe$ with x=0.225 is shown. On analysis of an ideal diffusion limited photodiode, we notice that the performance can be enhanced by optimizing the quantum efficiency and minimizing the reverse saturation current I_s. The saturation current for minority carriers can be give by equation 4.11. In this case the minority carriers are electrons on the p-side.

$$I_s = A\frac{qD_e n_{p0}}{L_e}\frac{\sinh\left(\frac{d}{L_e}\right) + \left(\frac{s_2 L_e}{D_e}\right)\cosh\left(\frac{d}{L_e}\right)}{\cosh\left(\frac{d}{L_e}\right) + \left(\frac{s_2 L_e}{D_e}\right)\sinh\left(\frac{d}{L_e}\right)} \tag{4.11}$$

It’s possible to minimize the leakage current from the side that does not contribute to the photo signal. If the doping or the bangap of the inactive side of the junction can be increases that in theory would reduce the leakage. If we place the back contact several diffusion lengths away such that $d \gg L_e$, then we would obtain:

$$I_s = \frac{qD_e n_{p0}}{L_e} A \quad (4.12)$$

As the back contact is brought closer to the junction the current can either increase or decrease depending on the surface recombination velocity greater than the diffusion velocity D_e/L_e. The performance of the device is strongly dependent on the properties of the back contact. Therefore the back contact is usually placed several diffusion lengths away from the junction or the contact itself is passivated or designed in such a way the surface recombination is low. For all our purposes we have considered surface recombination velocity at the front and back contact both to be zero.

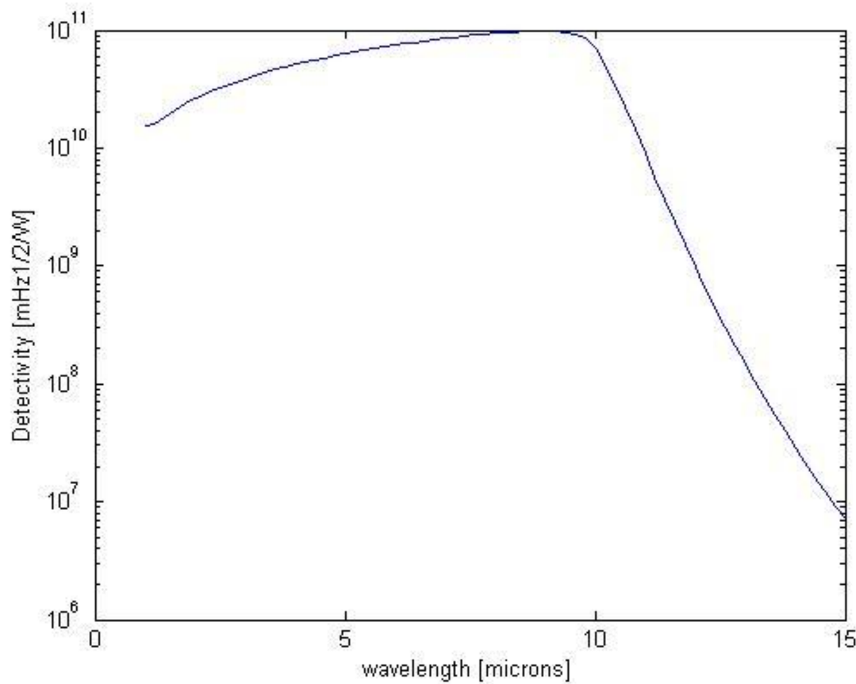

Fig 4.10: Detectivity vs. Wavelength.

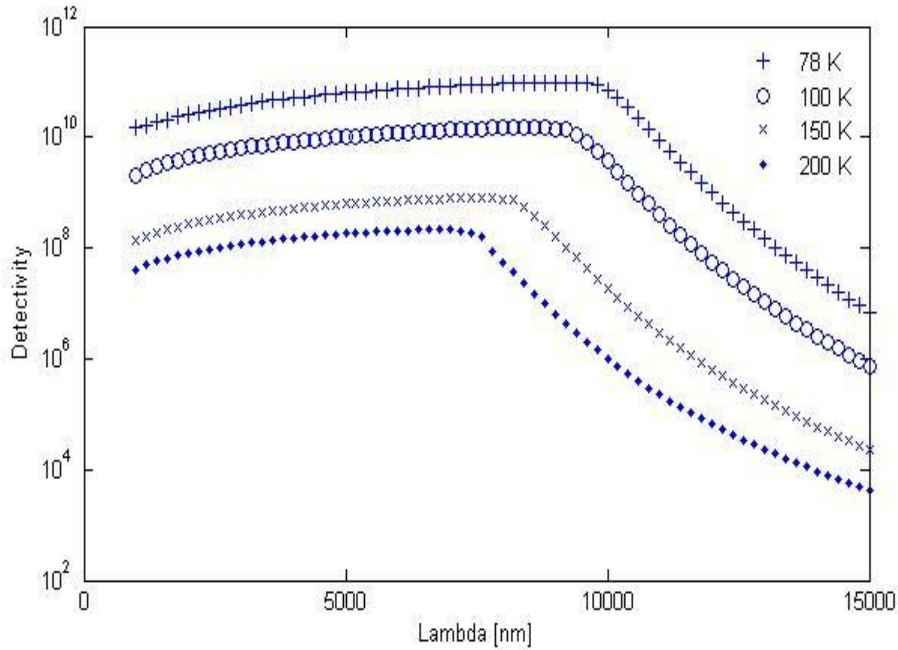

Fig 4.11: Detectivity vs. Wavelength at various temperatures.

Fig 4.11 shows us the various curves of detectivity vs wavelength of incident radiation at various temperatures. It is expected that the peak operating wave length will reduce as the bandgap increases with temperature, but it is also interesting to note how the magnitude of detectivity drops as temperature increases due to higher currents.

4.5. Carrier Freezeout

LWIR photodetectors are operated at liquid nitrogen temperatures to obtain the desired performance, this inevitable leads to partial ionization of the impurities or in other words 'carrier freezeout'. This not only reduces the carrier concentrations but has an effect on the lifetimes as well [27]. Fig.4.11 shows the p/N_a and n/N_d where $p \approx N_a^+$ and $n \approx N_d^+$ at equilibrium. In Fig.4.12 we see p/n_i and n/n_i. The information in these graphs give us a good idea about

the extent of carrier freezeout that takes place and the temperatures at which the device becomes intrinsic.

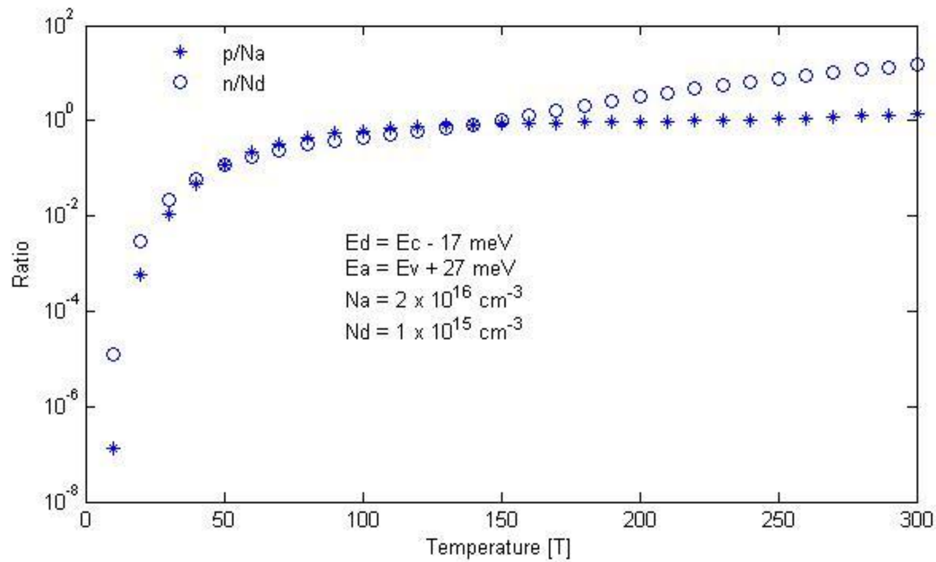

Fig 4.12: p/N_a and n/N_d vs. temperature.

In Fig.4.11 we see that at lower temperatures, the carrier concentrations are nowhere near the doping concentrations. The incomplete ionization of the dopants can also play an important factor in reducing the scattering at lower temperatures and thus increasing the mobility.

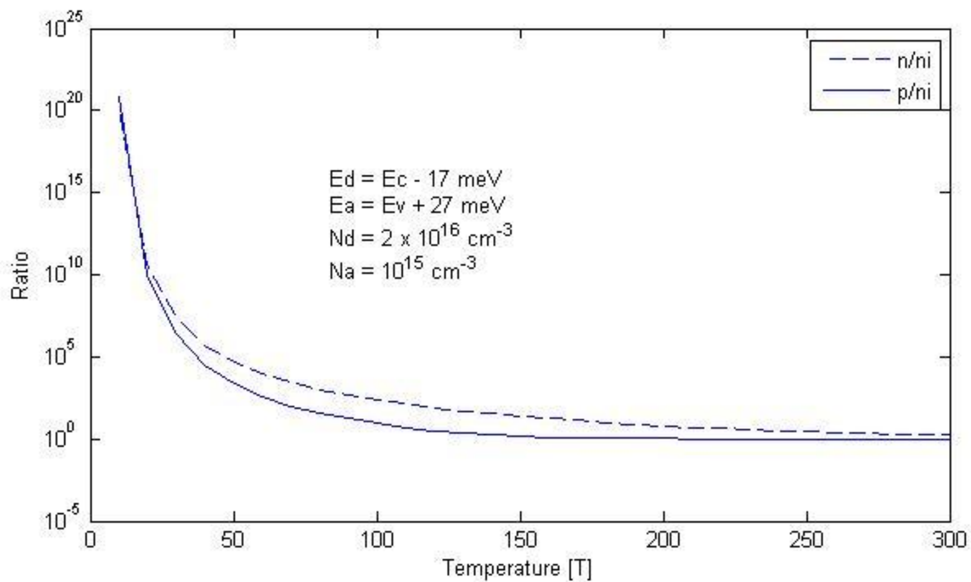

Fig 4.13: $n,p/n_i$ vs. Temperature.

We can see in Fig.4.12 that the ratio remains way below 1 for temperatures below 100 K signifying freezeout whereas $n,p/n_i$ near unity at room temperature signifying that the device is becoming intrinsic.

CONCLUSIONS AND FUTURE WORK

This thesis discusses the creation and implementation of a HgCdTe photodetector device simulator named 'OPTODET'. This simulator is also meant to be an educational tool, which will be deployed on nanohub.org. 'OPTODET' will give enable users to explore the characteristics of a HgCdTe photodetector by giving them the freedom to vary various device parameters. All simulations were done using MATLAB software provided by Mathworks Inc.

The primary aim of this thesis is to simulate key characteristics that determine the performance of a HgCdTe detector operating in the LWIR region. While modelling the dark current characteristics the importance of tunnelling through traps and band to band tunnelling has been realized. Complete Fermi-Dirac statistics have been implemented to accurately calculate electron and hole densities for degenerate and non-degenerate cases. Numerical methods such as LU decomposition and SOR method have been implemented to solve 1-D Poisson's equation. The SOR method was used for obtaining solutions at low temperatures (below 60K) as the LU method did not converge at those temperatures due to high oscillating error. As we know that the mole fraction in $Hg_{1-x}Cd_xTe$ can be varied to attain a desired bandgap. The tool discussed in this thesis is designed to operate for $0.2 \leq x \leq 0.6$ and $T > 50$ K. Even though the tool would be able to provide results below $T < 50$ K, the rate of convergence is slow at lower temperatures, therefore, leading to larger simulation times.

The lack of mature fabrication process still inhibits and undermines the progress of HgCdTe photodetectors. Historically the crystal growth of HgCdTe has been a major problem mainly because a relatively high Hg pressure is present during growth, which makes it difficult to control the stoichiometry and composition of the grown material.

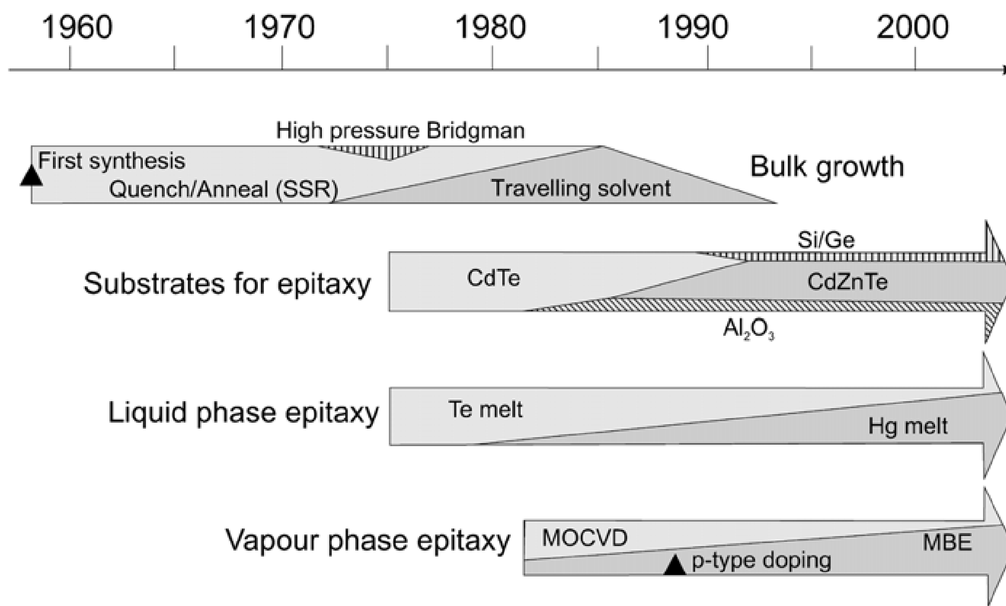

Fig.5.1: Evolution of HgCdTe crystal growth technology from 1958 to the present.

Fig.6.1 shows the evolution of fabrication techniques of HgCdTe. For the past decade considerable research has been directed towards epitaxial growth of HgCdTe. The epitaxial techniques offer, in comparison with bulk growth techniques, the possibility of growing large area epilayers and sophisticated device structures with good lateral homogeneity and abrupt and complex composition and doping profiles, which can be configured to improve the performance of the photodetectors. The growth is performed at low temperatures, which makes it possible to reduce the native defects density

[28]. Methods such as liquid phase epitaxy (LPE) and molecular beam epitaxy (MBE) have gained maturity in the past few years.

But in terms of detection of radiation in the infrared spectrum, HgCdTe is still a prominent material. Though the lack of a mature fabrication process coupled with the expensive operating cost that is incurred due to device operation at liquid nitrogen temperatures has prompted researchers to look for alternate materials for the purpose of infrared detection. $InAs/Ga_{1-x}In_xSb$ has been proposed for IR detector applications in the 8–14μm region [29]. Among different types of quantum well IR photodetectors (QWIPs) technology of the GaAs/AlGaAs multiple quantum well detectors is the most mature. The QWIP technology is relatively new and has been developed very quickly in the last decade [30-32] with LWIR imaging performance comparable to state-of-the-art of HgCdTe.

There are certain improvements that can be made to 'OPTODET' tool which can make a more complete and comprehensive educational tool. In the current version of this tool, we consider all regions of this device to have uniform cadmium concentration. This can be changed to include more novel device structures such as an $\underline{n}^+/\pi/\underline{p}^+$, where π is a lightly doped absorber layer and $\underline{n}^+$ and $\underline{p}^+$ are heavily doped wide gap n and p regions. The $\underline{n}^+ - \pi$ and $\underline{p}^+ - \pi$ when under reverse bias cause extraction of minority carriers in the lightly doped absorber layer (π). This will allow the flow of majority carriers out of the device while blocking the minority carriers.

Extending the ability of the tool to simulate heterojunction HgCdTe extraction diodes will be a great help in studying Auger suppressed diodes. A typical HgCdTe extraction diode has a wide gap n^+ layer, a lightly doped p

layer and another wide gap p^+ layer. The n-p interface is essentially an extraction junction for minority electrons, the p region is the extraction zone and the p-p interface is a non-recombining (excluding) contact for electrons. Auger Suppression (Auger-1 in n type HgCdTe and Auger-7 in p type HgCdTe) is extremely necessary as it is the dominant mechanism when we increase the device operating temperature. The suppression of this mechanism will play a significant role in achieving BLIP performance at higher temperatures.

REFERENCES

[1] Misra D., Brewer J., "Crystal radio detector ["cat's whisker"]: the first wireless device," Circuits and Devices Magazine, IEEE, vol.17, no.2, pp.12, (2001).

[2] McGill T.C. and Collins D.A., Semiconductor Science and Technology (1993).

[3] Bueno C.C, Goncalves J. A. C., de Magalhaes R. R., Santos M. D. S., Response of PIN diodes as room temperature photon detectors, Applied Radiation and Isotopes, Volume 61, Issue 6, Pages 1343-1347, (2004).

[4] Mizumoto I., Mashiko S., "Low noise near infrared detection system using InGaAs pin photodiode," Electronics Letters, vol.29, no.2, pp.234-236, (1993).

[5] Hussain, W., Rouf V.T., "Theoretical analysis of noise performance of an $In_{0.10}Ga_{0.90}Sb$ avalanche photodiode," First Asian Himalayas International Conference on , vol., no., pp.1-4, 3-5, (2009).

[6] Wang S., Sun X., Zheng X.G., Holmes A.L. Jr., Campbell J.C., Yuan P., "Avalanche photodiodes with an impact-ionization-engineered multiplication region," Lasers and Electro-Optics Society 2000 Annual Meeting, vol.1, pp.9-10, (2000)

[7] A.Krier, “Mid-infrared Semiconductor Optoelectronics”, Springer Series in Optical Sciences, Pages 3-8, (2006).

[8] “Narrow-gap II-VI Compounds for Optoelectronic and Electromagnetic Applications”, Electronic Materials Series, (1997).

[9] Rogalski A., “Infrared detectors at the beginning of the next millennium”, Opto-electronics review, 173-187, (2001).

[10] W. D. Lawson, S. Nielson, E. H. Putley, and A. S. Young, “Preparation and properties of HgTe and mixed crystals of HgTe-CdTe”, J. Phys. Chem. Solids vol. 9, 325–329, (1959).

[11] Roglaski A., Adamiec K., Rutkowski J., “Narrow-gap Semiconductor Photodiodes”, SPIE, (2000).

[12] “Semiconductor Device Theory I”, D. Vasileska, http://www.eas.asu.edu/~vasilesk/EEE531.html

[13] D.L. Scharfetter and H.K. Gummel, “Large signal analysis of a Silicon Read diode oscillator”, IEEE Trans. Electron Devices, vol. ED-16, pp. 64-77, (1969).

[14] Jean-Pierre Colinge and Cyntia A. Colinge, “Physics of Semiconductor Devices”, Springer Science+Business Media Inc., (2002).

[15] M.A Berding *et al.*, “SRH Lifetimes in HgCdTe”, (2004).

[16] G. A. M. Hurkx, D. B. M. Klaassen, M. P. *G.* Knuvers, and F. G. O’Hara, “A new recombination model describing heavy-doping effects and low- temperature behaviour,” in Proc. Int. Electron Device Meeting, pp. 307- 310., (1989).

[17] G. A. M. Hurkx, D. B. M. Klaassen, and M. P. G. Knuvers, “A New Recombination Model for Device Simulation Including Tunneling”, IEEE Transactions on Electron Devices, Vol. 39, No. 2, (1992).

[18] G. A. M. Hurkx, D. B. M. Klaassen, M. P. *G.* Knuvers, and F. G. O’Hara, “A new recombination model describing heavy-doping effects and low- temperature behaviour,” in Proc. Int. Electron Device Meeting, pp. 307- 310., (1989).

[19] Itsuno, A.M.; Phillips, J.D.; Velicu, S.; , "Predicted Performance Improvement of Auger-Suppressed HgCdTe Photodiodes and Heterojunction Detectors," Electron Devices, IEEE Transactions on , vol.58, no.2, pp.501-507, (2011)

[20] B. Li, J.H. Chu, Y. Chang, Y.S. Gui, and D.Y. Tang, “Optical absorption above the energy band gap in $Hg_x Cd_{1-x}Te$”, Infrared Phys. 32, (1991).

[21] E. Finkman and S.E. Schacham, “The exponential optical absorption band tail of $Hg_x Cd_{1-x}Te$ ”, J. Appl. Phys. 56, (1984).

[22] Z. Jianmin, F. Guobin and Z. Jun, “Characteristic of HgCdTe photoconductive detector in Energy Distribution System of Laser Spot in Far Field”, International Symposium on Photoelectronic Detection and Imaging, Proc. Of SPIE, Vol. 6621, (2008).

[23] Sang Dong Yoo and Kae Dal Kwack, “Theoretical Calculation of electron mobility in HgCdTe”, Aemrican Institute of Physics, (1997).

[24] Roglaski A., Adamiec K., Rutkowski J., “Narrow-gap Semiconductor Photodiodes”, SPIE, (2000).

[25] Jozwikowski, K.; Kopytko, M.; Rogalski, A.; Jozwikowska, A., "Enhanced numerical analysis of current-voltage characteristics of long wavelength infrared n-on-p HgCdTe photodiodes," Journal of Applied Physics , vol.108, no.7, pp.074519-074519-11,Oct2010.

[26] S. Krishnamurthy, M.A Berding, H. Robinson and A. Sher, “Tunneling in Long-Wavelength Infrared HgCdTe Photodiodes”, Journal of Electronic Materials, Vol. 35, No. 6, (2006).

[27] S.E Schacham and E. Finkman, “Recombination Mechanism in p-type HgCdTe: Freezeout and background flux effects”, Journal of Applied Physics, (1985).

[28] Antoni Rogalski, “Infrared Detectors: An Overview”, Infrared Physics & Technology 43, pages 187–210, (2002).

[29] F.Szmulowicz, F.L.Madarsz , Blocked impurity band detectors—An analytical model: Figures of merit, J.Appl.Phys.62, pages 2533–2540, (1987).

[30] Gunapala S.D. *et al., “*Recent developments and applications of quantum well infrared photodetector focal plane arrays”, Opto-Electron. Rev. **8**, pages 150–63, (2001).

[31] Schneider H., Koidl P., Walther M., Fleissner J., Rehm R., Diwo E., Schwarz K. and Weimann G., “Ten years of QWIP development at Fraunhofer”, Infrared Phys. Technol. 42, pages 283–9, (2001).

[32] Gunapala S.D., Bandara S.V., Liu J.K., Rafol B. and Mumolo J.M., “640×512 pixel long-wavelength infrared narrowband, multiband, and broadband QWIP focal plane arrays”, IEEE Trans. Electron Devices 50, (2004).